Microscopically implicit-macroscopically explicit schemes for the BGK equation

Original
Microscopically implicit-macroscopically explicit schemes for the BGK equation / Pieraccini, S., Puppo, G.. - In: JOURNAL OF COMPUTATIONAL PHYSICS. - ISSN 0021-9991. - STAMPA. - 231:2(2012), pp. 299-327. [10.1016/j.jcp.2011.08.027]

Publisher:
Elsevier

Published
DOI:10.1016/j.jcp.2011.08.027

Microscopically Implicit-Macroscopically Explicit schemes for the BGK equation *

Sandra Pieraccini, Gabriella Puppo †

July 25, 2011

Abstract

In this work a new class of numerical methods for the BGK model of kinetic equations is introduced. The schemes proposed are implicit with respect to the distribution function, while the macroscopic moments are evolved explicitly. In this fashion, the stability condition on the time step coincides with a macroscopic CFL, evaluated using estimated values for the macroscopic velocity and sound speed. Thus the stability restriction does not depend on the relaxation time and it does not depend on the microscopic velocity of energetic particles either. With the technique proposed here, the updating of the distribution function requires the solution of a *linear* system of equations, even though the BGK model is highly non linear. Thus the proposed schemes are particularly effective for high or moderate Mach numbers, where the macroscopic CFL condition is comparable to accuracy requirements. We show results for schemes of order 1 and 2, and the generalization to higher order is sketched.

Keywords: BGK model, kinetic equations, implicit schemes, hybrid methods.

AMS Subject Classifications: 65M06, 76P05, 82C80.

1 Introduction

This paper presents a new class of numerical schemes for the integration of the BGK model of kinetic equations. The schemes proposed here evolve implicitly the distribution function, which is the main variable in kinetic models, while computing an explicit evolution of macroscopic variables. Thus the schemes are explicit in the space time domain, while being implicit in phase space. With this technique, the Maxwellian equilibrium distribution is evolved explicitly, under a macroscopic CFL stability restriction, thus eliminating the main non linearity of the BGK model. Next, the evolution of the distribution function, containing non equilibrium information, is computed implicitly, solving an algebraic *linear system of equations*, which turns out to be well conditioned. In this fashion, we remove the stiffness due to small relaxation times *and* to high microscopic velocities. In the following, we illustrate the motivation and the background of the present work.

The BGK model [10] is an approximation to Boltzmann's equation which is the main tool for modeling rarefied gas regimes, characterized by a fluid behavior far from equilibrium conditions. In Boltzmann model, the fluid can be interpreted as a set of particles interacting through collisions. In the rarefied regime, the Knudsen number Kn, defined as the ratio between the mean free path λ of the particles and the characteristic dimension of the problem L ($\text{Kn} = \lambda/L$), is relatively large. Since equilibrium is approached through collisions, a large Knudsen number indicates a slow relaxation towards equilibrium.

---

[*] This work was supported by **PRIN 200774A7LH-002**

[†] Dipartimento di Matematica, Politecnico di Torino, corso Duca degli Abruzzi 24, 10129 Torino, Italia, e-mail: `sandra.pieraccini@polito.it`, `gabriella.puppo@polito.it`

Traditionally, the main field of application of Boltzmann equation has consisted in rarefied regimes, where the Knudsen number is large because the mean free path $\lambda \gg 1$, as in the upper layers of the atmosphere. More recently, rarefied regimes have attracted attention, because kinetic effects cannot be disregarded when the dimensions of the problem are so small that $L \simeq \lambda$, even for a gas in standard conditions, as in micro and nano devices, see for instance the recent book [30].

The main numerical method to integrate Boltzmann equation is the Direct Simulation Monte Carlo (DSMC) method, see for instance the classical reference [11]; more recent reviews can be found in [39, 37]. The DSMC scheme is based on the computation of collisions of a large number of sample particles, and it is exceedingly slow close to hydrodynamic regimes, when the number of collisions becomes very large. Moreover its results are polluted by stochastic noise and therefore lack smoothness. See [3] for a technique to reduce stochastic noise in kinetic regimes. On the other hand, in [18] information from the macroscopic equations is used to damp noise for small Knudsen numbers. Interest has also focused on deterministic methods, see for instance [38]. A recent review on numerical methods for Boltzmann equation is [40], see also references therein.

From a numerical point of view, the BGK [10, 13] model approximating Boltzmann equation for moderate Knudsen numbers is particularly attractive, because the collision integral is simplified. In fact, only precollisional microscopic velocities are involved, since the postcollisional distribution is assumed to be Maxwellian. Thus, only a precollisional velocity grid must be defined. It has a strong theoretical background, see for instance [41]. For the Boltzmann equation, the Chapman-Enskog expansion yields the system of compressible Euler equations for $\mathrm{Kn} \to 0$ and Navier Stokes equations for moderate Kn [14]. The same asymptotic procedure can be carried out for the BGK equations [47], yielding again the compressible Euler and the compressible Navier-Stokes equations, although with an incorrect Prandtl number. If the more sophisticated BGK-ES model [28] is used, the thermal conductivity coefficients can be recovered, [5, 6]. See also [44] for a recent work on the incompressible Navier Stokes limit of the BGK model and [48] for numerical applications, translating the BGK kinetic framework in the construction of reliable numerical schemes for Navier Stokes equations. Finally, Lattice Boltzmann schemes for Navier Stokes equations are based on a simplified BGK model, [45].

Extensive numerical computations have tested the potential of the BGK model to approximate Boltzmann solutions for moderate Kn and Euler solutions for $\mathrm{Kn} \ll 1$, see [16, 5] and [50]. The BGK model has also been used to evaluate several flows of physical interest, as gas mixtures, [4], reacting gas mixtures [36, 12], or phase change in kinetic regimes, [25, 8]. We also mention an application of BGK-like ideas to the development of models for the behaviour of fluids in nanostructures [27].

The importance of the BGK model in applications has prompted a parallel development of numerical methods tailored to the particular structure of BGK equations. We start mentioning the first order numerical scheme proposed in [16], and the linear second order scheme in [7, 8]. We also mention the third order in space scheme appearing in [50]. The schemes considered so far are not exactly conservative. This issue has been addressed in [34] and [35]. Exact conservation is obtained computing equilibrium at the discrete level. This construction requires the solution of a non linear system of 5 equations for the BGK model and 10 equations for the ES-BGK model at each grid point in space, even for explicit integration in time. A more recent method is proposed in [49].

All schemes described so far are either explicit or fully implicit. In the first case, the time step can be severely restricted by a small collision time, close to the hydrodynamic regime. In the second case, the fully implicit BGK equations result in a highly non linear large system of equations.

In [42] we proposed a high order scheme in both space and time to solve the BGK equations, based on an Implicit-Explicit Runge-Kutta scheme, see also [43]. In particular, the convective term is treated explicitly, unlike most numerical schemes for the BGK model in the stiff regime, while the source term is integrated implicitly, thus resolving the stiffness in the hydrodynamic regime. In the case of the BGK model, the implicit treatment of the collision term is very simple, because the local Maxwellian can be evaluated explicitly, see also [16]. This technique has been extended to the ES-BGK model in [24]. The main drawback of IMEX schemes for the BGK model is the fact that the stability condition depends on the fastest microscopic velocities of the grid, the high energy modes of [17]. This paper addresses also this convective stability restriction. The advantage of such IMEX schemes for the BGK model is that they can be proven to satisfy the AP (Asymptotic preserving) property defined in [29].

In the methods we propose here, we evolve explicitly in time the macroscopic variables, with a CFL stability restriction linked to the macroscopic velocity and local sound speed. The fluxes of the macroscopic equations are kinetic, but the fast microscopic modes are weighted with the corresponding values of the distribution function, and therefore their influence is limited, as in [17]. This allows to obtain the local Maxwellian explicitly, thus removing the non linearity of the BGK model. Once the Maxwellian is known, the BGK equation is linear in the distribution function f and can be integrated implicitly in time easily, at least for a first order scheme. At second order, even though the BGK equation is linear in f, the numerical flux functions are non linear to prevent the onset of spurious oscillations, see [33]. Here we describe a technique to obtain semi-linear numerical fluxes, which avoids the need to solve non linear systems of equations, as it occurs in current non oscillatory implicit schemes for conservation laws, see [22]. See also [20] for splitting fast and slow modes to address the stiffness of weakly compressible flows.

In many flows of physical interest, kinetic and hydrodynamic regimes co-exist, and recent multiscale approaches seek to solve the whole problem with a domain decomposition technique, where a hydrodynamic solver is used in equilibrium regions, while a kinetic solver is switched on in non equilibrium regimes. In [19] and [21] the kinetic model is given by the BGK equations, while the scheme for the hydrodynamic region can be any Euler solver. In [2] the ES-BGK model is used as an interface between equilibrium and highly non equilibrium regions, where the full Boltzmann equation is solved. In these cases, the present MiMe schemes provide the correct match for the hydrodynamic solver, since they permit to use the same time step all over the computational domain. Moreover, the BGK model can be used to remove the stiffness of the Boltzmann collision integral for small Knudsen numbers, [23]. In this case too MiMe schemes could provide a useful computational tool.

Finally, our MiMe schemes present similarities with the Micro-Macro approach of [32]. In that work the kinetic BGK system is split into an equilibrium (Maxwellian) and a non equilibrium equation, through the introduction of a projection operator on equilibrium and non equilibrium contributions. In our case, this projection is not needed, because the whole kinetic BGK equation is evolved, rather than computing and evolving the non equilibrium part. This permits to match easily the collisionless limit of high Knudsen numbers.

The paper is organized as follows. In Section 2 the BGK model is reviewed. The new MiMe schemes are described in Section 3, with details for the first and the second order case. We discuss the asymptotic behavior of MiMe schemes and of the IMEX scheme of [42] in §4, presenting also the space-time discretization of the schemes resulting for small Knudsen numbers, and discussing the AP property of the time discretization. Numerical results obtained with MiMe schemes are presented in Section 5, with a discussion on the entropic behavior of the schemes and the condition number of the implicit system. Finally, we end with a summary and perspectives for future work.

2 The BGK model

In this section, we introduce the equations defining the BGK model, recalling their main properties. For simplicity, we only consider the classical BGK model introduced in [10], using the notation of [16] and [34]. The scheme can be easily extended to more general BGK models.

We consider the initial value problem:

$$\begin{aligned} \frac{\partial f}{\partial t}(x,\, v,\, t) + v \cdot \nabla_x f(x,\, v,\, t) &= \frac{1}{\tau}(M_f(x,\, v,\, t) - f(x,\, v,\, t)) \qquad t \geq 0, \quad x \in \mathbb{R}^d, v \in \mathbb{R}^N \qquad (1) \\ f(x, v, 0) &= f_0(x, v) \geq 0 \qquad \text{given initial data.} \end{aligned}$$

We consider a monoatomic gas, which, in the general case, gives $d = 3$ and $N = 3$. In the 1D case, $d = 1$, $N = 3$ and $\nabla_x = (\partial_{x_1}, 0, 0)$. In (1) M_f is the Maxwellian obtained from the moments of f, namely:

$$M_f(x,\,v,\,t) = \frac{\rho(x,\,t)}{(2\pi RT(x,\,t))^{N/2}}\exp\left(-\frac{\|v-u(x,\,t)\|^2}{2RT(x,\,t)}\right).$$

The quantities ρ, u and T are respectively the macroscopic density, velocity and temperature of the gas, and they are obtained from the moments of f, defined below. Given any function $g : \mathbb{R}^N \mapsto \mathbb{R}$, let $\langle g\rangle$ be the quantity $\int_{\mathbb{R}^N} g(v)\,dv$; if $g : \mathbb{R}^N \mapsto \mathbb{R}^p$, $p > 1$, we still denote by $\langle g\rangle \in \mathbb{R}^p$ the vector whose components are given by $\langle g_i\rangle$. The moments of f are defined by

$$\begin{pmatrix} \rho \\ m \\ E \end{pmatrix}(x,t) = \langle f(x,\,v,\,t)\phi(v)\rangle\,, \qquad \text{with} \qquad \phi(v) = \begin{pmatrix} 1 \\ v \\ \frac{1}{2}\|v\|^2 \end{pmatrix}. \tag{2}$$

Here m is momentum, so that the macroscopic velocity is simply $u = m/\rho$, while E is the total energy, and the temperature is obtained from the internal energy e, through the relations: $\rho e = E - \frac{1}{2}\rho||u||^2$, $e = NRT/2$. In many applications, $N = 3$ which corresponds to a monoatomic gas with three translational degrees of freedom. In our tests, for simplicity, we will choose instead $N = 1$, as in [16]. This corresponds to a gas with a single degree of freedom, so that $e = RT/2$. The only difference with respect to a physical monoatomic gas appears in this rescaling of the temperature, which results, at equilibrium, in a γ-law gas, with $\gamma = 3$, where γ is the ratio of the specific heats. With this choice, all velocity integrals will be evaluated in $\mathbb{R}$ instead of $\mathbb{R}^3$. Another approach to reduce the computational complexity of the velocity integrals, while maintaining the physical properties of the gas, has been introduced in [15] and used, among others, in [8] and [50].

The parameter τ is the relaxation time, and it is a macroscopic quantity, i.e. $\tau = \tau(x,t)$. The collision frequency is τ^{-1}. In [8], $\tau^{-1} = A_c\rho$, where A_c is a given constant. In [34] the relaxation time is given by $\tau^{-1} = C\rho T^{1-\omega}$ where ω is the exponent of the viscosity law of the gas (for example, for argon one has $\omega = 0.81$).

In our tests, we will consider the adimensional case, for which:

$$\tau^{-1} = \frac{C}{\mathrm{Kn}}, \tag{3}$$

and we will take $C = 1$ as in [16]. However, we will write the scheme allowing for a dependence of τ on macroscopic variables.

The first macroscopic moments of f are conserved, in the sense that:

$$\partial_t\langle f\rangle + \nabla_x\cdot\langle fv\rangle = 0, \tag{4a}$$

$$\partial_t\langle fv\rangle + \nabla_x\cdot\langle v\otimes vf\rangle = 0, \tag{4b}$$

$$\partial_t\left\langle \frac{1}{2}\|v\|^2 f\right\rangle + \nabla_x\cdot\left\langle \frac{1}{2}\|v\|^2 vf\right\rangle = 0. \tag{4c}$$

Moreover, it is well known that for the BGK model an entropy principle holds, namely:

$$\partial_t\langle f\log f\rangle + \nabla_x\langle vf\log f\rangle \le 0, \qquad \forall f \ge 0, \tag{5}$$

the equality holding only for $f = M_f$.

A numerical scheme for (1) should be able not only to yield an accurate solution to equation (1), but also to satisfy the conservation equations and the entropy principle in some discretized form. Moreover, it is important that the scheme preserves the asymptotic limits of the BGK model. For $\tau \to 0$, $f \to M_f$, and the conservation laws (4) decay to the closed system of the compressible Euler equations of gas-dynamics.

For small values of τ, non equilibrium effects are still present, but a Chapman Enskog expansion shows that the asymptotic limit in this case coincides with the Compressible Navier-Stokes (CNS) equations, although the standard BGK model does not provide the correct Prandtl number. The correct asymptotic ratio between viscous and thermal effects is recovered by the ES-BGK model, see [5]. We will show that the scheme we propose naturally preserves the Euler limit of the BGK model and is consistent with the CNS asymptotics in §4, see also [9].

The BGK equation (1) is stiff if the relaxation time τ is small. Thus an explicit time integration of (1) would require very small time steps close to the hydrodynamic limit. On the other hand, the equation is highly non linear, so that an implicit solver might be computationally expensive. In [42] we have proposed an effective way to circumvent the stiffness of the collision term computing the Maxwellian explicitly and thus reducing the source term in (1) to a linear operator on f that can therefore be easily treated implicitly. This result has been obtained exploiting the properties of Implicit-Explicit (IMEX) schemes [31]. The application of IMEX schemes to the BGK equation is quite natural if the main stiffness of the problem is due to the relaxation term. This is the case of small relaxation times, when the flow is close to the hydrodynamic regime.

Another source of stiffness in (1) is due to the presence of high velocity modes in the convective term. The present work wishes to address both the convective and the relaxation stiffness of (1), without loosing the computational efficiency of [42]. The schemes outlined in [42] derive their time step restriction from the explicit part of the IMEX pair. Since the explicit part solves a linear convection problem, the time step restriction is given by the fastest modes in the convective terms, and these are given by the fastest microscopic velocity in the velocity grid. On the other hand, the fastest modes correspond to small values for f, thus it is quite natural to suppose that the macroscopic flow will not depend strongly on the fast velocity modes, see also [17]. For this reason, we would like to have a less severe CFL restriction, linked only to the macroscopic scales of the BGK equation. Furthermore, we want to keep the simplicity of the BGK-IMEX schemes [42] in the evaluation of the Maxwellian. More precisely, we want to build schemes which are AP (Asymptotic Preserving) in the sense of [29], i.e. schemes which are linear in the stiff non-linear terms, and that satisfy the correct asymptotics for small Knudsen numbers.

3 MiMe implicit schemes

The system (4) forms a non closed system of conservation laws, because the fluxes cannot be written as functions of the conserved variables. For the simple case of $N = 1$ (one degree of freedom in velocity space), the conservation laws can be written as:

$$\partial_t \rho + \nabla_x \cdot m = 0, \tag{6a}$$

$$\partial_t m + \nabla_x \cdot (2E) = 0, \tag{6b}$$

$$\partial_t E + \nabla_x \cdot \left\langle \frac{1}{2}\|v\|^2 v f \right\rangle = 0. \tag{6c}$$

These equations are not closed, because the energy flux depends on the unknown distribution f. For the case $N > 1$, even the momentum flux cannot be written as a function of conserved variables, but still the structure of the system is similar. Note that the dependence on the high velocity modes is weighted by the distribution f, which decays fast for large values of $|v|$. Thus we expect that the evolution of the macroscopic variables depends only weakly on the fast velocity modes. We rewrite the system above as:

$$\partial_t \mathbf{U} + \nabla_x \mathbf{F} = 0, \quad \mathbf{U} = \begin{pmatrix} \rho \\ m \\ E \end{pmatrix}, \quad \mathbf{F} = \mathbf{F}(\mathbf{U}, q) = \begin{pmatrix} m \\ 2E \\ q \end{pmatrix}, \quad \text{with } q = \left\langle \frac{1}{2}\|v\|^2 v f \right\rangle. \tag{7}$$

Since $\mathbf{U}$ and f are known at the beginning of each time step, we can integrate (7) using any available scheme for conservation laws, as long as we are able to estimate a stability condition and write a consistent numerical flux.

To achieve this goal, we note that the eigenvalues of the Jacobian of this system of equations will converge to the eigenvalues of the Euler equation, as $\tau \to 0$. To quantify this statement, we write f as a micro-macro decomposition, namely $f = M_f + \varepsilon g$, where M_f is as usual the Maxwellian corresponding to f, ε is a parameter of the same size of the Knudsen number, measuring the size of the relaxation time, and thus εg is the non equilibrium correction to M_f, which is not necessarily small, see for instance [9]. Introducing the peculiar velocity c, such that $v = u + c$, the last component of the flux can be written as:

$$\left\langle \frac{1}{2}\|v\|^2 v f \right\rangle = uE + \rho u RT + \left\langle \frac{1}{2}\|c\|^2 c f \right\rangle = uE + \rho u RT + \varepsilon \left\langle \frac{1}{2}\|c\|^2 c g \right\rangle,$$

since the third order moment of the Maxwellian is zero. It follows that the flux can be written as:

$$\mathbf{F} = \begin{pmatrix} m \\ 2E \\ uE + \rho u RT \end{pmatrix} + \varepsilon \begin{pmatrix} 0 \\ 0 \\ \langle \frac{1}{2}\|c\|^2 c g \rangle \end{pmatrix} = \mathbf{JF} \cdot \mathbf{U} + \varepsilon \begin{pmatrix} 0 \\ 0 \\ \langle \frac{1}{2}\|c\|^2 c g \rangle \end{pmatrix} \tag{8}$$

where $\mathbf{JF}$ is the Jacobian of $\mathbf{F}$ computed with respect to the variables $\mathbf{U}$ only. Thus the eigenvalues of the Jacobian can be computed as in the compressible Euler equations, within an approximation of order ε, as:

$$\lambda = u, u \pm C, \quad \text{where } C = \sqrt{\gamma RT}$$

is the local speed of sound, where in our simplified case $\gamma = 3$. Thus the approximation to the macroscopic CFL will be given by $\alpha = \max_x(|u| + C)$, and the stabilization of the numerical fluxes will rely on the estimate of the Jacobian of $\mathbf{F}$, based on $\mathbf{JF}$.

To construct a numerical flux function for equation (7), we need details on the solution of the Riemann problem for our kinetic flux function. A simpler approach is to use an approximate Riemann solver, which allows to construct a numerical flux, without the need to actually solve the Riemann problem. Some simple choices for the numerical flux will be given below.

Once the macroscopic equation has been integrated, the updated values of the moments are available. With these, we can compute the Maxwellian at the new time level. Note that in this fashion, the Maxwellian at the time t^{n+1} is computed with the macroscopic CFL, without solving non linear equations.

We now turn to the equation for f. We consider a generic implicit numerical scheme, such that the evolution of f will be computed as:

$$f^{n+1} = \mathcal{H}_{\Delta t}(f^n, M_f^n, f^{n+1}, M_f^{n+1}). \tag{9}$$

We note that we have already computed M_f^{n+1}. For a first order scheme, this is enough to provide a linear dependence of $\mathcal{H}_{\Delta t}$ on f^{n+1}. For a higher order scheme, $\mathcal{H}_{\Delta t}$ can depend non-linearly on f^{n+1}, but more details will follow. For the time being, we are ready to outline the structure of MiMe schemes for the BGK equation:

1. Solve the macroscopic equation (7) with any explicit Runge-Kutta scheme, using the stability estimate α for the CFL. Obtain the macroscopic moments $\mathbf{U}$ at the new time t^{n+1}.
2. Compute the updated Maxwellian M_f^{n+1}, using the new moments $\mathbf{U}^{n+1}$.
3. Solve for f^{n+1} the time-discretized equation for f, (9).

Note that, unlike [9], we solve the macroscopic equation *and* the full kinetic equation for f. This avoids the need to compute the linearized collision operator and its projections.

Before describing the complete structure of the schemes we propose, we first define the computational grid. We consider a velocity grid defined on Gauss Hermite nodes, centered around typical values of the macroscopic variables appearing in the initial condition. In this case, the grid is non uniform, and the quadrature for the velocity integrals is a Gaussian quadrature; for the details, see [1]. We will denote by $v_k, k = 1, \ldots, N_v$ the generic velocity node of the velocity grid. The discretization in space is based on a uniform discretization, with mesh spacing h. We will not address the difficult problem of boundary conditions in this work, but we will consider compactly supported initial data, with free flow boundary conditions. The generic node in space will be labelled as $x_j, j = 1, \ldots, N_{\mathrm{x}}$. The grid value of a macroscopic variable will be denoted as $\mathbf{U}(x_j, t^n) = \mathbf{U}_j^n$, while the function f in phase space evaluated at a grid node will be written as $f(x_j, v_k, t^n) = f_{kj}^n$. The moments of f computed with the velocity quadrature rule will be written as:

$$\langle \phi f \rangle_{N_v}(x, t) = \sum_k w_k \phi(v_k) f(x, v_k, t),$$

where v_k and w_k are the nodes and weights of the quadrature rule. Finally, $\lambda = \Delta t/h$ will denote the mesh ratio.

First order MiMe scheme

We start from the first order MiMe scheme. The integration of (7) is carried out with the explicit Euler scheme while the space discretization is written in conservation form. Thus:

$$\mathbf{U}_j^{n+1} = \mathbf{U}_j^n - \lambda \left[\mathcal{F}_{j+1/2} - \mathcal{F}_{j-1/2} \right], \tag{10}$$

where $\mathcal{F}_{j+1/2}$ is the numerical flux function, which is a function of the values of the solution across the interface $\mathcal{F}_{j+1/2} = \mathcal{F}(\mathbf{U}_{j+1}, q_{j+1}; \mathbf{U}_j, q_j)$. With this formulation, the macroscopic moments computed in (10) are exactly conserved, because they are computed with a conservative scheme. So, provided that the numerical solution converges under grid refinement, then the limit solution is a weak solution of (7) by the Lax-Wendroff theorem.

The simplest numerical flux function is based on Lax Friedrichs flux splitting:

$$\mathcal{F}_{j+1/2} = \mathcal{F}(\mathbf{U}_{j+1}, q_{j+1}; \mathbf{U}_j, q_j) = \mathbf{F}^+(\mathbf{U}_j, q_j) + \mathbf{F}^-(\mathbf{U}_{j+1}, q_{j+1}). \tag{11}$$

The functions $\mathbf{F}^+$ and $\mathbf{F}^-$ are estimates of the positive and negative parts of the flux and are given by:

$$\mathbf{F}^+(\mathbf{U}, q) = \frac{1}{2}\left(\mathbf{F}(\mathbf{U}, q) + \alpha \mathbf{U}\right), \qquad \mathbf{F}^-(\mathbf{U}, q) = \frac{1}{2}\left(\mathbf{F}(\mathbf{U}, q) - \alpha \mathbf{U}\right). \tag{12}$$

In this fashion, the simple estimate α for the local CFL will also provide the means to write a numerical flux function for the kinetic flux. Here, α can be computed as a function of x and t as $\alpha(x, t) = |u(x, t)| + C(x, t)$, giving the Local Lax Friedrichs flux splitting, or we can choose a global value for α as $\alpha(t) = \max_x(|u(x, t)| + C(x, t))$, yielding the Global Lax Friedrichs flux splitting, which will be used in most of our tests. Lax Friedrichs numerical flux is very robust and simple, but it is quite diffusive.

In this work we also considered the less diffusive HLL flux, see for instance [46]. In this case:

$$\mathcal{F}(\mathbf{U}_{j+1}, q_{j+1}; \mathbf{U}_j, q_j) = \begin{cases} \mathbf{F}(\mathbf{U}_j, q_j) & s^-_{j+1/2} > 0 \\ \frac{s^+_{j+1/2}\mathbf{F}(\mathbf{U}_j, q_j) - s^-_{j+1/2}\mathbf{F}(\mathbf{U}_{j+1}, q_{j+1})}{s^+_{j+1/2} - s^-_{j+1/2}} & \\ \qquad - \frac{s^+_{j+1/2} s^-_{j+1/2}}{s^+_{j+1/2} - s^-_{j+1/2}}(\mathbf{U}_{j+1} - \mathbf{U}_j) & s^-_{j+1/2} < 0 < s^+_{j+1/2} \\ \mathbf{F}(\mathbf{U}_{j+1}, q_{j+1}) & s^+_{j+1/2} < 0 \end{cases} \tag{13}$$

where $s^+_{j+1/2}$ and $s^-_{j+1/2}$ are estimates of the local characteristic speeds, namely:

$$s^+_{j+1/2} = \max(u_j + C_j, u_{j+1} + C_{j+1}) \qquad s^-_{j+1/2} = \min(u_j - C_j, u_{j+1} - C_{j+1}).$$

The literature on numerical flux functions is huge [46], and many other choices are possible. Another interesting possibility is the kinetic flux splitting used, among others, in [9] or [48].

Once the updated macroscopic moments are available, we compute a discrete Maxwellian as:

$$(M_U)^{n+1}_{kj} = M(\mathbf{U}^{n+1})(x_j, v_k, t^{n+1}) = \frac{\rho^{n+1}_j}{(2\pi R T^{n+1}_j)^{N/2}} \exp\left(-\frac{\|v_k - u^{n+1}_j\|^2}{2RT^{n+1}_j}\right). \tag{14}$$

This is an approximate Maxwellian in the sense that $\langle \phi M_U \rangle_{N_v} \simeq \mathbf{U}$, with an error depending on the accuracy of the quadrature rule. To achieve the equality sign, it is necessary to compute an exact discrete Maxwellian as in [34]. However, in general the difference between the approximate and the exact discrete Maxwellians are much below the truncation error of the scheme, expecially when the moments are computed with Gauss-Hermite quadrature, see also [1] and Tables 4 and 5. From the updated moments, we also compute the new relaxation time $\tau^{n+1}_j = \tau(\mathbf{U}^{n+1}_j)$.

We can now integrate the equation for f. We obtain a system of N_v partial differential equations. Note that only the equations corresponding to high velocity nodes, i.e. values of v_k such that $|v_k| > \alpha$ need to be integrated implicitly. Accordingly, let $\theta_k = 0$ if $|v_k| \leq \alpha$ while $\theta_k = 1$ if $|v_k| > \alpha$. The discrete (in time and velocity) equation for f is:

$$f^{n+1}_k(x) = f^n_k(x) - \Delta t \theta_k \partial_x(v_k f^{n+1}_k) - \Delta t(1-\theta_k)\partial_x(v_k f^n_k) + \frac{\Delta t}{\tau^{n+1}_j(x)}(M^{n+1}_k(x) - f^{n+1}_k(x)). \tag{15}$$

Finally, the space discretization is given by first order upwinding. Let $v^+_k = \max(v_k, 0)$ and $v^-_k = \min(v_k, 0)$. Then the first order scheme for f takes the form:

$$\begin{aligned} f^{n+1}_{kj} &= f^n_{kj} - \lambda\theta_k \left(v^+_k(f^{n+1}_{kj} - f^{n+1}_{k,j-1}) + v^-_k(f^{n+1}_{k,j+1} - f^{n+1}_{kj})\right) + \\ & -\lambda(1-\theta_k)\left(v^+_k(f^n_{kj} - f^n_{k,j-1}) + v^-_k(f^n_{k,j+1} - f^n_{kj})\right) + \frac{\Delta t}{\tau^{n+1}_j}(M^{n+1}_{kj} - f^{n+1}_{kj}). \end{aligned}$$

The implicit scheme is linear in f^{n+1} and can be rewritten as:

$$\begin{aligned} &\left(1 + \frac{\Delta t}{\tau^{n+1}_j} + \lambda\theta_k|v_k|\right) f^{n+1}_{kj} - \lambda\theta_k v^+_k f^{n+1}_{k,j-1} + \lambda\theta_k v^-_k f^{n+1}_{k,j+1} = \\ &f^n_{kj} - \lambda(1-\theta_k)\left(v^+_k(f^n_{kj} - f^n_{k,j-1}) + v^-_k(f^n_{k,j+1} - f^n_{kj})\right) + \frac{\Delta t}{\tau^{n+1}_j} M^{n+1}_{kj} \end{aligned} \tag{16}$$

Thus the coefficient matrix of the algebraic system is tridiagonal. Its structure will be more complex in the general $N > 1$ case, but it still enjoys a high degree of sparsity. We will see in the numerical results section that the condition number of the matrix arising from system (16) is small, so that an iterative linear solver will converge in a few iterations. Note also that the implicit equations will be solved only for the fast microscopic velocities, for the first order scheme.

Second order MiMe scheme

To extend these ideas to higher order schemes, we will illustrate mainly the second order case, where most of the difficulties already appear. For simplicity, we will suppose that the time integration will be implicit for all velocity nodes. The integration of the macroscopic equation (7) will be carried out with a ν stages explicit Runge-Kutta scheme:

$$\mathbf{U}^{n+1}_j = \mathbf{U}^n_j - \lambda \sum_{i=1}^{\nu} b_i \left[\mathcal{F}^{(i)}_{j+1/2} - \mathcal{F}^{(i)}_{j-1/2}\right], \tag{17}$$

where the numerical fluxes at the i-th stage require the predictor steps:

$$\mathbf{U}_j^{(i)} = \mathbf{U}_j^n - \lambda \sum_{l=1}^{i-1} a_{il} \left[\mathcal{F}_{j+1/2}^{(l)} - \mathcal{F}_{j-1/2}^{(l)} \right], \tag{18}$$

where the coefficients $b_i, i = 1, \ldots, \nu$ and $a_{i,l}, i, l = 1, \ldots, \nu$ define the ν stages of the Runge-Kutta scheme. Here we are using an explicit Runge-Kutta scheme, so $a_{i,l} = 0$ for $l \geq i$. The evaluation of the numerical flux $\mathcal{F}$ at the i-th stage requires knowledge of the distribution function $f^{(i)}$, which is not available. It is well known, see [26], that each explicit Runge-Kutta scheme can be written as a combination of explicit Euler steps:

$$\begin{aligned} \mathbf{U}_j^{(1)} &= \mathbf{U}_j^n \\ \mathbf{U}_j^{(i+1)} &= \sum_{l=1}^{i} \alpha_{i,l} \left(\mathbf{U}_j^{(l)} + \Delta t \frac{\beta_{i,l}}{\alpha_{i,l}} \frac{1}{h} \left[\mathcal{F}_{j-1/2}^{(l)} - \mathcal{F}_{j+1/2}^{(l)} \right] \right), \qquad i = 1, \ldots, \nu \\ \mathbf{U}_j^{n+1} &= \mathbf{U}_j^{(\nu+1)}, \end{aligned} \tag{19}$$

where the coefficients $\alpha_{i,l} \geq 0$ and $\beta_{i,l} \geq 0$ can be computed from the coefficients b_i and $a_{i,l}$ of the usual Butcher tableaux. Clearly, for consistency, $\sum_l \alpha_{i,l} = 1$, so (19) shows that each $\mathbf{U}^{(i)}$ is obtained as a convex combination of i forward Euler steps. It is the particular combination of these Euler steps that yields the desired accuracy, see [26]. In our case, we are interested in a second order scheme. In particular we choose the TVD second order Heun scheme which can be written in the form (19) as follows:

$$\begin{aligned} \mathbf{U}_j^{(1)} &= \mathbf{U}_j^n \\ \mathbf{U}_j^{(2)} &= \mathbf{U}_j^{(1)} + \Delta t \frac{1}{h} \left[\mathcal{F}_{j-1/2}^{(1)} - \mathcal{F}_{j+1/2}^{(1)} \right] \\ \mathbf{U}_j^{n+1} &= \mathbf{U}_j^{(3)} = \frac{1}{2} \mathbf{U}_j^{(1)} + \frac{1}{2} \left[\mathbf{U}_j^{(2)} + \Delta t \frac{1}{h} \left[\mathcal{F}_{j-1/2}^{(2)} - \mathcal{F}_{j+1/2}^{(2)} \right] \right]. \end{aligned} \tag{20}$$

To compute $\mathbf{U}^{(2)}$ we need only information available from the previous time step. Note that $\mathbf{U}^{(2)}$ is obtained evolving $\mathbf{U}^{(1)}$ for a single Forward Euler step with time step Δt. Then from $\mathbf{U}^{(2)}$ we compute $M^{(2)} = M(\mathbf{U}^{(2)})$, and we evaluate $f^{(2)}$ with Backward Euler as:

$$\frac{f^{(2)} - f^n}{\Delta t} = -v \partial_x f^{(2)} + \frac{1}{\tau} \left(M^{(2)} - f^{(2)} \right).$$

Now $f^{(2)}$ is available at the same time level of $\mathbf{U}^{(2)}$. With this information, the numerical kinetic fluxes $\mathcal{F}^{(2)}$ can be computed giving the macroscopic moments $\mathbf{U}^{n+1}$ through the last equation of (20), completing the update of macroscopic variables.

The space discretization is again based on the construction of a numerical flux except that the numerical flux is now applied to reconstructed values at the cell edges, namely:

$$\mathcal{F}_{j+1/2} = \mathcal{F}(\mathbf{U}_{j+1/2}^+, q_{j+1/2}^+; \mathbf{U}_{j+1/2}^-, q_{j+1/2}^-). \tag{21}$$

where $\mathbf{U}_{j+1/2}^+$ and $\mathbf{U}_{j+1/2}^-$ are the solution values extrapolated to the cell edges, with, for instance, a piecewise polynomial reconstruction, matching the accuracy of the Runge-Kutta scheme. For second order accuracy, we use a piecewise linear reconstruction:

$$\mathbf{U}_{j+1/2}^+ = \mathbf{U}_j + \frac{1}{2} \sigma_j \qquad \mathbf{U}_{j+1/2}^- = \mathbf{U}_j - \frac{1}{2} \sigma_j, \tag{22}$$

where σ_j is a non oscillatory reconstructed slope, for instance:

$$\sigma_j = \mathrm{MM}\left(\mathbf{U}_{j+1} - \mathbf{U}_j, \mathbf{U}_j - \mathbf{U}_{j-1}\right),$$

where MM denotes the MinMod function, see [33]. The same reconstruction is applied on q. This piecewise linear reconstruction is second order accurate on smooth flows and away from extrema, where the limiter built in the MinMod function degrades accuracy to first order. This mechanism prevents the onset of spurious oscillations, which might develop with shock formation, see again [33]. In conservation laws, one would reconstruct only conserved variables, namely, density, momentum and total energy. Here however these variables are not enough to define the flux, and a new macroscopic variable needs to be reconstructed, in this case, the heat flux.

To update the distribution function, we distinguish between the stage values of f which must be computed during the advection of macroscopic variables, and the actual update of f after the new Maxwellian has been computed, at the end of the integration of the macroscopic conserved variables. Again, we consider the second order case.

The stage values are computed with the implicit Euler scheme. This scheme is highly diffusive and limiting may not be necessary. When this is the case, as for the smooth test used for the convergence history of the scheme, the slopes are obtained with central differences:

$$\sigma_j = \frac{f_{j+1} - f_{j-1}}{2}.$$

Then, using second order implicit upwinding, and recalling that $v_k^+ - v_k^- = |v_k|$ and $v_k^+ + v_k^- = v_k$, we find the linear system:

$$\begin{aligned}\left(1 + \frac{3}{4}\lambda|v_k| + \frac{\Delta t}{\tau_j^{(2)}}\right) f_{kj}^{(2)} + \lambda\left(v_k^- + \frac{1}{4}v_k\right) f_{k,j+1}^{(2)} - \lambda\left(v_k^+ + \frac{1}{4}v_k\right) f_{k,j-1}^{(2)} \\ + \frac{\lambda}{4} v_k^+ f_{k,j-2}^{(2)} - \frac{\lambda}{4} v_k^- f_{k,j+2}^{(2)} = f_{kj}^n + \Delta t \frac{(M_U)_{kj}^{(2)}}{\tau_j^{(2)}}.\end{aligned} \tag{23}$$

Thus $f^{(2)}$ is first order accurate in time and second order accurate in space. Note that the coefficient matrix is now pentadiagonal: as usual, when accuracy increases, the sparsity of the system decreases. This approach however may lead to spurious oscillations when discontinuities in space arise. To prevent this problem slopes should be limited; however, the use of slope limiting introduces nasty non linearities which require a non linear solver for the resulting system of equations, see [22]. To avoid this problem, we first estimate $f^{(2)}$ with $\tilde{f}^{(2)}$ computed with a first order accurate in space upwind scheme. Thus, $\tilde{f}^{(2)}$ is non oscillatory but it is only first order accurate. We use this estimate to compute the stencil used by the MinMod function applied to $\tilde{f}^{(2)}$. In this fashion we obtain a semi-linear recipe to compute the limited slopes. More precisely, let f be the unknown function for which the limited slopes are needed, and let $\tilde{f}$ be the predicted value of f which is used to compute the stencil. We construct the limited slopes as follows:

$$\sigma_j(f, \tilde{f}) = \begin{cases} 0 & \text{if } s_j = (\tilde{f}_{j+1} - \tilde{f}_j)(\tilde{f}_j - \tilde{f}_{j-1}) \le 0 \\ f_j - f_{j-1} & \text{if } s_j > 0 \quad \text{and} \quad |\tilde{f}_{j+1} - \tilde{f}_j| > |\tilde{f}_j - \tilde{f}_{j-1}| \\ f_{j+1} - f_j & \text{if } s_j > 0 \quad \text{and} \quad |\tilde{f}_{j+1} - \tilde{f}_j| < |\tilde{f}_j - \tilde{f}_{j-1}|. \end{cases} \tag{24}$$

Note that $\sigma(f, \tilde{f})$ is linear in f and it is a first order accurate approximation of the slope of f away from extrema.

We introduce the space difference operator $\mathcal{L}_h(f, \sigma(f, \tilde{f}))$ which approximates $hv \cdot \nabla_x f$:

$$\mathcal{L}_h(f, \sigma(f, \tilde{f}))\Big|_{kj} = |v_k| f_{kj} - v_k^+ f_{k,j-1} + v_k^- f_{k,j+1} + \frac{1}{2}\left(v_k \sigma_{kj} - v_k^+ \sigma_{k,j-1} - v_k^- \sigma_{k,j+1}\right). \tag{25}$$

We are now ready to compute the stage value $f^{(2)}$ which is given by the linear system:

$$\left(1 + \frac{\Delta t}{\tau^{(2)}}\right) f^{(2)} + \lambda \mathcal{L}_h\left(f^{(2)}, \sigma(f^{(2)}, \tilde{f}^{(2)})\right) = f^n + \frac{\Delta t}{\tau^{(2)}} M_U^{(2)}. \tag{26}$$

This completes the second order space-time discretization of the scheme for macroscopic variables.

Next, the update values f^{n+1} are computed with Crank-Nicolson scheme, which has a small amplitude error even at high CFL's. Since this scheme has no dissipation, limiting the slopes is recommended, and the limited slopes are computed via (24) using the already available $f^{(2)}$ as predictor, namely $\sigma = \sigma(f^{n+1}, f^{(2)})$. Therefore,

$$\begin{aligned}\left(1 + \frac{\Delta t}{2\tau^{n+1}}\right) f^{n+1} + \frac{\lambda}{2} \mathcal{L}_h\left(f^{n+1}, \sigma(f^{n+1}, f^{(2)})\right) \quad = \quad & \left(1 + \frac{\Delta t}{2\tau^{n}}\right) f^{n} - \frac{\lambda}{2} \mathcal{L}_h\left(f^{n}, \sigma(f^{n}, f^{n})\right) \\ & + \frac{\Delta t}{2}\left(\frac{1}{\tau^{n+1}} M_U^{n+1} + \frac{1}{\tau^n} M_U^n\right). \end{aligned} \tag{27}$$

In this fashion, we still obtain a linear system of equations for the grid values of f^{n+1}.

Remark 3.1 (Limiting) Limiting is necessary for the piecewise linear reconstruction of macroscopic moments in the second order scheme, while integrating the macroscopic equations. If limiters are omitted, spurious oscillations do develop in the presence of singularities in space in the solution. In our tests, limiting is not crucial in the evaluation of the slopes of the distribution function f in the Crank Nicolson update of f^{n+1}, although this might be problem dependent, while in our experience limiting is not necessary in the Backward Euler step to compute $f^{(2)}$, because the implicit Euler scheme provides enough dissipation to contrast the onset of oscillations.

Remark 3.2 (Higher order) To achieve high order, we must match the order of the space and time discretizations. High order explicit Runge-Kutta can be used for macroscopic variables, in the form (19), finding the corresponding values of $f^{(l)}$ through Backward Euler integration with suitable time steps depending on the coefficients of the scheme. The numerical kinetic fluxes $\mathcal{F}^{(l)}$ will be computed using high order non oscillatory space reconstructions, such as WENO or ENO. Finally f^{n+1} can be computed through a BDF or a Diagonally Implicit Runge-Kutta scheme.

Realigning moments

In regimes close to equilibrium, when $\tau \ll 1$, the microscopic equation for f reduces to a relaxation to the local Maxwellian. Thus, the macroscopic equations become a closed system of equations for the moments $\mathbf{U}$. When we are far away from equilibrium the moments $\mathbf{U}$ do depend on f and not only on the Maxwellian. However, in the schemes described so far we have

$$\mathbf{U}^{n+1} = \mathbf{U}(f^n, \mathbf{U}^n).$$

To force dependence of $\mathbf{U}^{n+1}$ on f^{n+1}, we correct the moments obtained by the macroscopic equations by computing the moments of the new distribution function. Namely:

$$\mathbf{U}^{n+1} = \left\langle f^{n+1} \phi \right\rangle. \tag{28}$$

This operation will be called *moments realignment* and it enforces a stronger coupling between f and its moments. Since this operation is necessary only away from equilibrium, we perform moments realignment following an adaptive strategy. We define the local Knudsen number as in [11]:

$$\mathrm{Kn}_{\mathrm{loc}}(x,t) = \frac{\lambda}{L(x,t)}, \qquad L(x,t) = \frac{\rho}{\rho_x}(x,t) \tag{29}$$

and we set

$$\mathbb{K}(t) = \max_x \mathrm{Kn}_{\mathrm{loc}}(x,t). \tag{30}$$

When $\mathbb{K}(t)$ is larger than a given tolerance TOL, moments realignment is performed. A local in space adaptive strategy would introduce spurious singularities in the moments and therefore it might produce small oscillations.

We end this section reporting a sketch of the two algorithms just described.

Algorithm 1 ***MiMe1***

```
1. Given $f_0$, compute $\mathbf{U}^0$ using quadrature, $\tau^0$ and the Maxwellian $M_f^0$.
2. For $n = 0, 1, \ldots$
    • Compute $q^n = \left\langle \frac{1}{2}\|v\|^2 v f^n \right\rangle$
    • Compute $\mathbf{U}^{n+1}$ integrating (7) with (10)
    • Update the relaxation time $\tau^{n+1}$ and the Maxwellian $M_f^{n+1}$.
    • Compute $f^{n+1}$ via (16)
    • If needed, realign moments: $\mathbf{U}^{n+1} = \left\langle f^{n+1}\phi \right\rangle$.
```

Algorithm 2 ***MiMe2***

```
1. Given $f_0$, compute $\mathbf{U}^0$ using quadrature, $\tau^0$ and the Maxwellian $M_f^0$.
2. For $n = 0, 1, ...$
    • Compute $q^n = \left\langle \frac{1}{2}\|v\|^2 v f^n \right\rangle$
    • Compute $\mathbf{U}^{n+1}$ integrating (7) with (20) (Heun RK scheme):
        – Compute boundary extrapolated data $\mathbf{U}^{(1),+}$ and $\mathbf{U}^{(1),-}$, $q^{(1),+}$ and $q^{(1),-}$ with (22)
        – Compute new stage values $\mathbf{U}^{(2)}$ via (20) with $\mathcal{F}^{(1)} = \mathcal{F}(\mathbf{U}^{(1),+}, q^{(1),+}; \mathbf{U}^{(1),-}, q^{(1),-})$ as in (21)
        – Update the relaxation time $\tau^{(2)}$ and the Maxwellian $M_f^{(2)}$
        – Predict the stage value $f^{(2)}$ with the implicit Euler scheme and second order implicit upwinding (23) or (26)
        – Compute $q^{(2)} = \left\langle \frac{1}{2}\|v\|^2 v f^{(2)} \right\rangle$
        – Compute boundary extrapolated data $\mathbf{U}^{(2),+}$ and $\mathbf{U}^{(2),-}$, $q^{(2),+}$ and $q^{(2),-}$ with (22)
        – Compute the new moments $\mathbf{U}_j^{n+1}$ via (20)
    • Update the relaxation time $\tau^{n+1}$ and the Maxwellian $M_f^{n+1}$.
    • Compute $f^{n+1}$ via (27)
    • If needed, realign moments: $\mathbf{U}^{n+1} = \left\langle f^{n+1}\phi \right\rangle$
```

4 BGK schemes and Navier-Stokes asymptotics

In this section we wish to prove that the schemes proposed in this work become schemes for the Compressible Euler equation for Kn → 0, while they are consistent with the Compressible Navier Stokes (CNS) equations for small Kn. The key aspect here is the time discretization, since it is at this level that the macroscopic and the microscopic equations are coupled. Thus, for simplicity, we will compute the asymptotics for the semidiscrete in time version of the scheme. More precisely we will compute the asymptotic behavior for the first order in time IMEX scheme of [42], since this was not considered in our previous work, and for the first order in time MiMe scheme, with and without moments realignement. For completeness, we will also compute the space discretization the scheme reduces to for small Knudsen numbers, and the behavior for time steps much larger that the relaxation time, when the initial layer is not resolved.

As in [9], we consider a constant relaxation time, and we write instead of τ, $\varepsilon\tau$, where $\varepsilon = \mathrm{Kn}$ is the small parameter. In this section, for simplicity, we will take the gas constant $R = 1$. With this notation, the CNS equations corresponding to one degree of freedom in the microscopic velocity are:

$$\partial_t \begin{pmatrix} \rho \\ m \\ E \end{pmatrix} + \partial_x \begin{pmatrix} m \\ 2E \\ \frac{m}{\rho}(E + \rho T) \end{pmatrix} = \varepsilon \partial_x \begin{pmatrix} 0 \\ 0 \\ \frac{3}{2}\tau \rho T \partial_x T \end{pmatrix} \tag{31}$$

BGK-IMEX scheme

The first order in time semidiscrete BGK-IMEX scheme of [42] can be written as:

$$f^{n+1} = f^n - \Delta t v \partial_x f^{(1)} + \frac{\Delta t}{\varepsilon \tau}\left(M^{(1)} - f^{(1)}\right) \tag{32}$$

$$f^{(1)} = f^n + \frac{\Delta t}{\varepsilon \tau}\left(M^{(1)} - f^{(1)}\right). \tag{33}$$

From this, we find that the evolution equation for the macroscopic moments is obtained computing moments of (32), which gives:

$$\mathbf{U}^{n+1} = \mathbf{U}^n - \Delta t \left\langle v\phi \partial_x f^{(1)} \right\rangle. \tag{34}$$

We define the kinetic correction $g^{(1)}$ to the Maxwellian $M^{(1)}$ as: $f^{(1)} = M^{(1)} + \varepsilon g^{(1)}$. Note that $\left\langle \phi(v) g^{(1)} \right\rangle = 0$. Substituting this expression in (32), we find the first order Chapman-Enskog correction to the Maxwellian, namely:

$$g^{(1)} = -\frac{\tau}{\Delta t}\left(M^{n+1} - M^n\right) - \tau v \partial_x M^n + O(\varepsilon) \tag{35}$$

since $M^{(1)} = M^n$ for this scheme, and the macroscopic equation (34) becomes:

$$\mathbf{U}^{n+1} = \mathbf{U}^n - \Delta t \left\langle v\phi \partial_x M^n \right\rangle + \varepsilon \tau \Delta t \left(\partial_x \left\langle v\phi \frac{M^{n+1} - M^n}{\Delta t} \right\rangle + \partial^2_{xx} \left\langle v^2 \phi M^n \right\rangle \right) + O(\varepsilon)^2. \tag{36}$$

Clearly, as $\varepsilon \to 0$, eq. (36) becomes a semidiscrete approximation of the Compressible Euler equations, since $\langle v\phi M^n \rangle$ is the macroscopic equilibrium flux. Denote with CE the vector of the Chapman-Enskog correction defined by the expression inside the parenthesis in the equation above. For the first component, $\phi = 1$ and we find:

$$\mathrm{CE}_1 = \partial_x \frac{m^{n+1} - m^n}{\Delta t} + \partial^2_{xx}(2E^n) = 0,$$

thanks to (34). The second component of CE has $\phi = v$ and we find:

$$\mathrm{CE}_2 = 2\partial_x \frac{E^{n+1} - E^n}{\Delta t} + \partial^2_{xx} \left\langle v^3 M^n \right\rangle,$$

using the semidiscrete energy equation, we find:

$$\mathrm{CE}_2 = -2\partial^2_{xx} \left\langle \frac{1}{2} v^3 M^n \right\rangle - \varepsilon \partial^2_{xx} \left\langle v^3 g^{(1)} \right\rangle + \partial^2_{xx} \left\langle v^3 M^n \right\rangle$$

which now gives an $O(\varepsilon)$ correction:

$$\mathrm{CE}_2 = -\varepsilon \partial^2_{xx} \left\langle v^3 g^{(1)} \right\rangle. \tag{37}$$

Finally, the third component has $\phi = \frac{1}{2}v^2$, and we note that there is no conservation law for $\left\langle \frac{1}{2} v^3 M \right\rangle$, so we will expand this expression in time, namely:

$$\begin{aligned}
\mathrm{CE}_3 &= \partial_x \left\langle \frac{1}{2} v^3 \frac{M^{n+1} - M^n}{\Delta t} \right\rangle + \partial^2_{xx} \left\langle \frac{1}{2} v^4 M^n \right\rangle \\
&= \frac{1}{2} \partial_x \frac{(\rho u^3 + 3\rho u T)^{n+1} - (\rho u^3 + 3\rho u T)^n}{\Delta t} + \frac{1}{2} \partial^2_{xx} \left(3\rho T^2 + 6\rho u^2 T + \rho u^4\right) \\
&= \frac{1}{2} \partial_x \left[\partial_t \left(\rho u^3 + 3\rho u T\right)^n + \partial_x \left(3\rho T^2 + 6\rho u^2 T + \rho u^4\right)^n \right] + O(\Delta t),
\end{aligned}$$

where we have used the fact that $\left\langle v^3 M \right\rangle = \rho u^3 + 3\rho u T$ and $\left\langle v^4 M \right\rangle = \rho u^4 + 6\rho u^2 T + 3\rho T^2$. Expanding the time derivatives, and using the evolution equation of conserved quantities, we find:

$$\mathrm{CE}_3 = \frac{3}{2}\partial_x \left(\rho T \partial_x T\right) - \varepsilon 3 u \partial_x \left\langle v^3 g^{(1)} \right\rangle + O(\Delta t). \tag{38}$$

Thus the semidiscrete first order in time IMEX scheme is consistent with the equations:

$$\frac{\mathbf{U}^{n+1} - \mathbf{U}^n}{\Delta t} + \partial_x \begin{pmatrix} m \\ 2E \\ \frac{m}{\rho}(E + \rho T) \end{pmatrix} = \varepsilon \partial_x \begin{pmatrix} 0 \\ 0 \\ \frac{3}{2}\tau \rho T \partial_x T \end{pmatrix} + O(\varepsilon \Delta t) + O(\varepsilon^2) \tag{39}$$

which is consistent with the correct equation as $\Delta t \to 0$, within $O(\varepsilon^2)$ terms.

MiMe scheme

We consider the first order in time semidiscrete MiMe scheme. In the first time step, we set $U^0 = \left\langle \phi f^0 \right\rangle$, where $f^0 = f(\cdot, \cdot, t = 0)$. We write $M^n = M(\mathbf{U}^n)$, where $M(\mathbf{U})$ is the Maxwellian built with the moments $\mathbf{U}$. Then the semidiscrete in time first order scheme can be written as:

$$\begin{aligned} \frac{\mathbf{U}^{n+1} - \mathbf{U}^n}{\Delta t} &= -\partial_x \begin{pmatrix} m^n \\ 2E^n \\ \left\langle \frac{1}{2} v^3 f^n \right\rangle \end{pmatrix} \\ M^{n+1} &= M(\mathbf{U}^{n+1}) \\ \frac{f^{n+1} - f^n}{\Delta t} &= -v \partial_x f^{n+1} + \frac{1}{\varepsilon \tau}\left(M^{n+1} - f^{n+1}\right). \end{aligned}$$

In this case, M^n and f^n do not have exactly the same moments, but as $\varepsilon \to 0, f^n \to M^n$. Thus we can still decompose f in its equilibrium and kinetic part: $f^n = M^n + \varepsilon g^n$, but this time $\langle \phi g \rangle \neq 0$. Still, we can compute the first order kinetic correction starting from the equation for f, finding:

$$g^{n+1} = -\frac{\tau}{\Delta t}\left(M^{n+1} - M^n\right) - \tau v \partial_x M^{n+1} + O(\varepsilon) \tag{40}$$

Substituting the kinetic correction in the equation for the macroscopic quantities, we find that the first two components are exact, while for the third component:

$$\mathrm{CE}_3 = \partial_x \left\langle \frac{1}{2} v^3 \frac{M^n - M^{n-1}}{\Delta t} \right\rangle + \partial^2_{xx} \left\langle \frac{1}{2} v^4 M^n \right\rangle = \partial_x \partial_t \left\langle \frac{1}{2} v^3 M^n \right\rangle + \partial^2_{xx} \left\langle \frac{1}{2} v^4 M^n \right\rangle + O(\Delta t),$$

so that we find the same expression of eq. (38) within $O(\Delta t)$ terms. So again the semidiscrete scheme is consistent with the CNS equations for small ε.

MiMe scheme with moments realignement

This time, we consider the first order in time semidiscrete MiMe scheme with moments realignement. In this case, we are only given f^n. The scheme can be written as:

$$\begin{aligned} \widetilde{\mathbf{U}}^n &= \langle \phi f^n \rangle \\ \frac{\mathbf{U}^{n+1} - \widetilde{\mathbf{U}}^n}{\Delta t} &= -\partial_x \begin{pmatrix} \widetilde{m}^n \\ 2\widetilde{E}^n \\ \left\langle \frac{1}{2} v^3 f^n \right\rangle \end{pmatrix} \\ M^{n+1} &= M(\mathbf{U}^{n+1}) \\ \frac{f^{n+1} - f^n}{\Delta t} &= -v \partial_x f^{n+1} + \frac{1}{\varepsilon \tau}\left(M^{n+1} - f^{n+1}\right). \end{aligned}$$

Again, M^n and f^n do not have exactly the same moments, but as $\varepsilon \to 0, f^n \to M^n$. Thus we can still decompose f in its equilibrium and kinetic part: $f = M + \varepsilon g$, but recalling that $\langle \phi g \rangle \neq 0$. Still, we can compute the first order kinetic correction starting from the equation for f, and we find the same expression of (40). Substituting the kinetic correction in the equation for the macroscopic quantities, we find:

$$\frac{\mathbf{U}^{n+1} - \mathbf{U}^n}{\Delta t} = -\left\langle v\phi\partial_x M^n \right\rangle + \varepsilon\tau \left(\partial_x \left\langle v\phi \frac{M^n - M^{n-1}}{\Delta t} \right\rangle + \partial^2_{xx} \left\langle v^2 \phi M^n \right\rangle \right) + \frac{\widetilde{\mathbf{U}}^n - \mathbf{U}^n}{\Delta t} + O(\varepsilon)^2$$

We need to evaluate $\widetilde{\mathbf{U}}^n - \mathbf{U}^n$. To this end, we compute moments of the evolution equation for f^{n+1}, and we subtract the result from the evolution equation for $\mathbf{U}^{n+1}$, finding:

$$\frac{\mathbf{U}^{n+1} - \widetilde{\mathbf{U}}^{n+1}}{\Delta t} = \frac{\varepsilon\tau}{\varepsilon\tau + \Delta t} \partial_x \left\langle v\phi \left(f^{n+1} - f^n \right) \right\rangle . \tag{41}$$

Substituting this information in the equation for the macroscopic variables, we have:

$$\frac{\mathbf{U}^{n+1} - \mathbf{U}^n}{\Delta t} = -\partial_x \left\langle v\phi f^n \right\rangle - \frac{\varepsilon\tau}{\varepsilon\tau + \Delta t} \partial_x \left\langle v\phi (f^n - f^{n-1}) \right\rangle . \tag{42}$$

Since the kinetic correction g still has the same form as for the original MiMe scheme, the first term is consistent with the CNS equations for small ε, while the second term is $O(\Delta t)$ and thus is of the same order as the truncation error of the scheme. On the other hand, if we consider the evolution equation for $\widetilde{\mathbf{U}}$, we have:

$$\frac{\widetilde{\mathbf{U}}^{n+1} - \widetilde{\mathbf{U}}^n}{\Delta t} = -\partial_x \left\langle v\phi f^{n+1} \right\rangle + \frac{\Delta t}{\varepsilon\tau + \Delta t} \partial_x \left\langle v\phi (f^{n+1} - f^n) \right\rangle . \tag{43}$$

In other words, if $\varepsilon \to 0$, we recover the evolution equation of MiMe scheme. If on the other hand ε is not too small, then the effect of realignement is to add an implicit term to the integration of the equation for macroscopic moments, thus increasing its stability region.

Space discretization and Chapman-Enskog expansion

In this subsection, we analyze the space discretization induced by MiMe first order scheme on the macroscopic equations, when ε is small. We rewrite the first order MiMe scheme with the Lax-Friedrichs numerical flux for the macroscopic equation, and the upwind discretization for the kinetic equation, i.e.

$$\frac{U_j^{n+1} - U_j^n}{\Delta t} = -\frac{1}{\Delta x} \left(\mathcal{F}^n_{j+1/2} - \mathcal{F}^n_{j-1/2} \right) \tag{44}$$

$$\frac{f_j^{n+1} - f_j^n}{\Delta t} = -\frac{v^+}{\Delta x} \left(f_j^{n+1} - f_{j-1}^{n+1} \right) - \frac{v^-}{\Delta x} \left(f_{j+1}^{n+1} - f_j^{n+1} \right) + \frac{1}{\varepsilon\tau} \left(M_j^{n+1} - f_j^{n+1} \right) , \tag{45}$$

where the index j denotes the j-th space cell. Write f separating its equilibrium part as $f = M + \varepsilon g$, supposing again that g is bounded, so that as $\varepsilon \to 0$, f decays to its corresponding equilibrium Maxwellian. Then, the Lax-Friedrichs numerical flux can be written as:

$$\mathcal{F}_{j+1/2} = \frac{1}{2} \left(\left\langle \phi(v) v M \right\rangle_{j+1} + \left\langle \phi(v) v M \right\rangle_j - \alpha (U_{j+1} - U_j) \right) + \frac{\varepsilon}{2} \left(\left\langle \phi(v) v g \right\rangle_{j+1} + \left\langle \phi(v) v g \right\rangle_j \right) ,$$

where α is the discretization parameter of the Lax-Friedrichs flux, and $\phi(v)$ is the vector of collision invariants. Clearly, as $\varepsilon \to 0$, the expression above reduces to the usual Lax-Friedrichs flux of the compressible Euler equations, irrespective of the kinetic equation. Thus, we recover, even at the level of the space discretization, a scheme for the compressible Euler equations. Note also that an analogous behavior would hold for the other numerical fluxes considered before. Let us split the macroscopic flux into its equilibrium and kinetic correction as $\mathcal{F}_{j+1/2} = F^E_{j+1/2} + \varepsilon F^K_{j+1/2}$, where F^E is clearly the part that depends only on the Maxwellian, while F^K is the part depending on g,

Now, we wish to study the first order in ε kinetic correction. Substituting $f = M + \varepsilon g$ in (45), we find the first order kinetic correction:

$$g^n_j = \tau \frac{M^n_j - M^{n-1}_j}{\Delta t} + \frac{\tau v^+}{\Delta x}(M^n_j - M^n_{j-1}) + \frac{\tau v^-}{\Delta x}(M^n_{j+1} - M^n_j) + O(\varepsilon^2) \tag{46}$$

Then the kinetic correction to the numerical flux can be written as:

$$\begin{aligned} F^K_{j+1/2} = {} & \frac{1}{2}\left(\left\langle \phi(v) v \frac{M^n_{j+1} - M^{n-1}_{j+1}}{\Delta t}\right\rangle + \left\langle \phi(v) v \frac{M^n_j - M^{n-1}_j}{\Delta t}\right\rangle\right) \\ & + \frac{1}{2}\left(\left\langle \phi(v) v v^+ \frac{M^n_{j+1} - M^n_j}{\Delta x}\right\rangle + \left\langle \phi(v) v v^- \frac{M^n_{j+2} - M^n_{j+1}}{\Delta x}\right\rangle\right) \\ & + \frac{1}{2}\left(\left\langle \phi(v) v v^+ \frac{M^n_j - M^n_{j-1}}{\Delta x}\right\rangle \left\langle \phi(v) v v^- \frac{M^n_{j+1} - M^n_j}{\Delta x}\right\rangle\right) \end{aligned} \tag{47}$$

In our approach, the first two components of the flux can be written entirely in terms of macroscopic variables. However, if we wish to emphasize the kinetic correction, we would have, for $\phi(v) = 1$:

$$\begin{aligned} F^K_{1,j+1/2} = {} & \frac{1}{2}\left(\frac{m^n_{j+1} - m^{n-1}_{j+1}}{\Delta t} + \left\langle v v^+ \frac{M^n_{j+1} - M^n_j}{\Delta x}\right\rangle + \left\langle v v^- \frac{M^n_{j+2} - M^n_{j+1}}{\Delta x}\right\rangle\right) \\ & + \frac{1}{2}\left(\frac{m^n_j - m^{n-1}_j}{\Delta t} + \left\langle v v^+ \frac{M^n_j - M^n_{j-1}}{\Delta x}\right\rangle + \left\langle v v^- \frac{M^n_{j+1} - M^n_j}{\Delta x}\right\rangle\right) \end{aligned}$$

The two parenthesis are both first order discretizations of the momentum equation with an upwind kinetic flux, computed respectively in the cell $j+1$ and in the cell j. So both terms are $O(\Delta t) + O(\Delta x)$. When we add this contribution to the macroscopic equation for the density, we must consider the flux difference, so that the kinetic contribution to the macroscopic equation is $O(\varepsilon((\Delta t) + (\Delta x)^2)) + O(\varepsilon^2)$. An analogous argument holds for the momentum equation, except that, in this case, the kinetic correction contains discretizations of the energy equation.

The energy equation has a kinetic correction to the numerical flux given by:

$$\begin{aligned} F^K_{j+1/2} = {} & \frac{1}{4}\left(\left\langle v^3 \frac{M^n_{j+1} - M^{n-1}_{j+1}}{\Delta t}\right\rangle + \left\langle v^3 \frac{M^n_j - M^{n-1}_j}{\Delta t}\right\rangle\right) \\ & + \frac{1}{2}\left(\left\langle v^3 v^+ \frac{M^n_{j+1} - M^n_j}{\Delta x}\right\rangle + \left\langle v^3 v^- \frac{M^n_{j+2} - M^n_{j+1}}{\Delta x}\right\rangle\right) \\ & + \frac{1}{2}\left(\left\langle v^3 v^+ \frac{M^n_j - M^n_{j-1}}{\Delta x}\right\rangle \left\langle v^3 v^- \frac{M^n_{j+1} - M^n_j}{\Delta x}\right\rangle\right) \end{aligned} \tag{48}$$

The evaluation of the integrals above is quite cumbersome. However it is easy to get a representation of the terms discretized by the expressions above. The second and the third line of the equation are first order discretizations of $\langle \partial_x v^4 M_{j+1}\rangle$ and $\langle \partial_x v^4 M_j\rangle$ respectively, obtained with a kinetic flux splitting. Expanding M^{n-1} in time, we find:

$$F^K_{j+1/2} = \frac{1}{4}\left(\langle \partial_t v^3 M_{j+1}\rangle + \langle \partial_x v^4 M_{j+1}\rangle + \langle \partial_t v^3 M_j\rangle + \langle \partial_x v^4 M_j\rangle\right) + O(\Delta t) + O(\Delta x). \tag{49}$$

We recall that, for one degree of freedom in velocity space, $\langle \partial_t v^3 M\rangle + \langle \partial_x v^4 M\rangle = 3\rho T \partial_x T$. Thus the kinetic correction to the evolution of the energy equation is:

$$\varepsilon\left(F^K_{j+1/2} - F^K_{j-1/2}\right) = \frac{\varepsilon}{2}\left(\frac{3}{2}\rho T \partial_x T\Big|_{j+1} - \frac{3}{2}\rho T \partial_x T\Big|_{j-1}\right) + O(\varepsilon^2) + O(\varepsilon \Delta t) + O(\varepsilon \Delta x)^2 \tag{50}$$

which amounts to a first order in time, second order in space central discretization of the CNS heat flux.

AP property and large integration time steps

In this section we wish to investigate the convergence to the relaxed state, when the time step is much larger than the relaxation time.

We start from the space homogeneous case, since this property is essentially determined by the time discretization of the scheme. In this case, the BGK equation reduces to:

$$\partial_t f = \frac{1}{\varepsilon\tau}\left(M_f - f\right), \tag{51}$$

where again we have emphasized the dependence on the small parameter ε In the space homogeneous case, the moments are conserved, so $\mathbf{U}^{n+1} = \mathbf{U}^n$, so that the Maxwellian is also conserved: ${M_f}^{n+1} = {M_f}^n$. The first order scheme can be written as:

$$f^{n+1} = \frac{1}{1+\frac{\Delta t}{\varepsilon\tau^{n+1}}} f^n + \frac{\frac{\Delta t}{\varepsilon\tau^{n+1}}}{1+\frac{\Delta t}{\varepsilon\tau^{n+1}}} {M_f}^{n+1}.$$

For $\Delta t >> \varepsilon$, we expand in power of ε, obtaining:

$$\begin{aligned} f^{n+1} &= \frac{\varepsilon\tau^{n+1}}{\Delta t}\left(1 - \frac{\varepsilon\tau^{n+1}}{\Delta t} + O(\frac{\varepsilon\tau^{n+1}}{\Delta t})^2\right) f^n + \left(1 - \frac{\varepsilon\tau^{n+1}}{\Delta t} + O(\frac{\varepsilon\tau^{n+1}}{\Delta t})^2\right) {M_f}^{n+1} \\ &= {M_f}^{n+1} + O(\varepsilon), \end{aligned}$$

independently of the initial data. Thus, when the time step is too large to resolve the relaxation process, the distribution function decays on the Maxwellian even for not well prepared data.

For the second order case, the macroscopic moments are still conserved, together with all macroscopic dependent quantities. Starting again from (51), MiMe scheme reduces to:

$$\frac{1}{1+\frac{\Delta t}{2\varepsilon\tau^{n+1}}} f^{n+1} = \frac{1}{1-\frac{\Delta t}{2\varepsilon\tau^{n+1}}} f^n + \frac{\Delta t}{\varepsilon\tau^{n+1}} {M_f}^{n+1}.$$

Expanding again in ε, we have:

$$f^{n+1} = 2M^{n+1} - f^n + O(\varepsilon).$$

For well prepared data $f^n = M^n + O(\varepsilon) = M^{n+1} + O(\varepsilon)$, so that the scheme satisifes the weak *AP* property of [29]. The stronger AP property can be obtained using an L-stable time integrator, such as a DIRK scheme, instead of the Crank-Nicolson scheme. Note that moments realignement does not help. On the other hand, in the space non homogeneous case, extra diffusion in time is provided by the backward Euler advancement of f in the prediction of macroscopic variables, which drives the system towards equilibrium. As a matter of fact, well prepared data are not needed in the solution of Riemann problems with MiMe2 to converge to the correct compressible Euler solution, even for $\Delta t >> \varepsilon$.

5 Numerical results

In this section we illustrate the characteristics of MiMe schemes using a few benchmark problems. We consider a smooth test problem, where the distribution function is locally Maxwellian, but with a macroscopic velocity depending on x (Test 1), see also [42]. Next we consider three Riemann problems. The first one (Test 2) was proposed in [16]. The second Riemann problem is Lax' Riemann problem, with $\gamma = 3$, which is a quite hard classical test problem in gas dynamics. In this case, we will also investigate the collisionless limit of the numerical solution. The third problem [9] yields a stationary shock, and it is useful to compute the shock structure and compare the kinetic and Compressible Navier Stokes solutions. Finally, a space homogeneous problem is considered, in order to investigate the dependence of the initial layer on Kn.

	MiMe1			BGK1		
	Kn $= 10^{-1}$					
N_{x}	ρ	u	T	ρ	u	T
40	1.868e-03	2.243e-03	1.720e-03	2.640e-03	2.211e-03	4.731e-03
80	1.102e-03	1.088e-03	1.666e-03	1.488e-03	1.217e-03	2.675e-03
160	4.821e-04	5.460e-04	1.332e-03	7.834e-04	6.381e-04	1.437e-03
320	2.433e-04	3.080e-04	8.125e-04	4.014e-04	3.262e-04	7.486e-04
640	1.217e-04	1.716e-04	4.509e-04	2.032e-04	1.651e-04	3.825e-04
	Kn $= 10^{-2}$					
N_{x}	ρ	u	T	ρ	u	T
40	1.781e-03	1.936e-03	2.315e-03	2.628e-03	2.282e-03	5.494e-03
80	1.034e-03	8.771e-04	1.470e-03	1.486e-03	1.261e-03	3.171e-03
160	4.368e-04	3.883e-04	7.254e-04	7.844e-04	6.645e-04	1.706e-03
320	2.207e-04	2.045e-04	4.027e-04	4.025e-04	3.403e-04	8.903e-04
640	1.104e-04	1.091e-04	2.128e-04	2.041e-04	1.725e-04	4.556e-04
	Kn $= 10^{-5}$					
N_{x}	ρ	u	T	ρ	u	T
40	1.639e-03	1.750e-03	3.271e-03	2.593e-03	2.508e-03	6.620e-03
80	9.250e-04	8.357e-04	1.839e-03	1.475e-03	1.414e-03	3.941e-03
160	3.786e-04	3.464e-04	7.470e-04	7.841e-04	7.602e-04	2.155e-03
320	1.952e-04	1.749e-04	3.837e-04	4.041e-04	3.952e-04	1.130e-03
640	9.892e-05	8.803e-05	1.943e-04	2.054e-04	2.020e-04	5.798e-04

Table 1: Test 1, absolute errors under grid refinement in space and time, MiMe1 vs BGK1

Test 1 Smooth test. We start with an initial distribution of the kind [42]:

$$f(x,v,0) = \frac{\rho}{\sqrt{2\pi RT}} \cdot \exp\left(-\frac{(v-u_0(x))^2}{2RT}\right), \qquad x \in [-1,1],$$

with constant density $\rho = 1$ and temperature $T = 1$ and with

$$u_0(x) = \frac{1}{\sigma}\left(\exp\left(-(\sigma x - 1)^2\right) - 2\exp\left(-(\sigma x + 3)^2\right)\right)$$

with $\sigma = 10$. Thus initially the distribution function f is smooth, with a localized perturbation in velocity, in a gas with a uniform density and temperature.

Test 2 Coron-Perthame Riemann problem. We take as initial data a distribution which is discontinuous in space:

$$f(x,v,0) = \begin{cases} \rho_L(2\pi RT_L)^{-1/2} \cdot \exp(-\frac{(u_L-v)^2}{2RT_L}), & 0 \leq x \leq 0.5, \\ \rho_R(2\pi RT_R)^{-1/2} \cdot \exp(-\frac{(u_R-v)^2}{2RT_R}), & 0.5 < x \leq 1 \end{cases} \tag{52}$$

with $(\rho_L, u_L, T_L) = (2.25, 0, 1.125)$ and $(\rho_R, u_R, T_R) = (3/7, 0, 1/6)$. This test is derived from [16].

Test 3 Lax' Riemann problem. Again, we take as initial data a distribution discontinuous in space of the form (52), on the interval $-3 < x < 3$ and with the discontinuity located in the middle. In this case, the parameters in (52) are given by: $(\rho_L, (\rho u)_L, E_L) = (0.4450, 0.311, 8.928)$, $(\rho_R, (\rho u)_R, E_R) = (0.5, 0, 1.4275)$, $p = (E - \frac{1}{2}(\rho u)^2/\rho)(\gamma - 1)$ and $T = p/(R\rho)$. This test corresponds to Lax' problem, with $\gamma = 3$.

	MiMe2			BGK2		
	Kn = 10^{-1}					
N_{x}	ρ	u	T	ρ	u	T
40	1.379e-03	1.908e-03	1.594e-03	1.467e-03	1.560e-03	2.895e-03
80	2.878e-04	4.615e-04	5.967e-04	3.847e-04	4.463e-04	9.384e-04
160	1.933e-05	2.130e-05	4.981e-05	8.545e-05	1.164e-04	2.476e-04
320	5.799e-06	5.225e-06	9.207e-06	1.837e-05	3.181e-05	6.012e-05
640	1.737e-06	1.311e-06	1.884e-06	6.464e-06	1.138e-05	1.630e-05
	Kn = 10^{-2}					
N_{x}	ρ	u	T	ρ	u	T
40	1.339e-03	1.811e-03	2.473e-03	1.445e-03	1.698e-03	3.260e-03
80	2.627e-04	4.861e-04	5.496e-04	3.816e-04	4.941e-04	1.080e-03
160	6.292e-05	1.272e-04	1.429e-04	9.446e-05	1.469e-04	2.977e-04
320	1.672e-05	2.671e-05	4.019e-05	2.233e-05	4.003e-05	7.647e-05
640	4.630e-06	5.728e-06	1.131e-05	5.469e-06	1.060e-05	1.922e-05
	Kn = 10^{-5}					
N_{x}	ρ	u	T	ρ	u	T
40	1.394e-03	2.092e-03	2.891e-03	1.506e-03	1.911e-03	4.148e-03
80	2.998e-04	7.053e-04	6.189e-04	4.765e-04	6.303e-04	1.305e-03
160	7.194e-05	2.221e-04	1.480e-04	1.612e-04	2.622e-04	4.050e-04
320	1.703e-05	5.685e-05	3.485e-05	4.745e-05	8.113e-05	1.110e-04
640	4.126e-06	1.428e-05	8.412e-06	1.240e-05	2.184e-05	2.779e-05

Table 2: Test 1, absolute errors under grid refinement in space and time, MiMe2 vs BGK2

N_{x}	MiMe1	BGK1	MiMe2	BGK2
Gauss-Hermite quadrature, $N_{\mathrm{v}} = 21$				
40	0.0388	0.0557	0.0711	0.0996
80	0.0826	0.1815	0.2155	0.3548
160	0.2101	0.7174	0.7837	1.4137
320	0.8955	3.3577	4.2644	7.2667
640	5.2198	21.2364	29.7991	42.8896
Gauss-Hermite quadrature, $N_{\mathrm{v}} = 41$				
40	0.0626	0.1147	0.1270	0.2159
80	0.1349	0.3786	0.3808	0.7536
160	0.3771	1.6872	1.4869	3.4321
320	1.5795	9.0798	9.0705	17.6198
640	8.8954	53.4511	61.9136	108.7406

Table 3: Test 1, CPU times.

Test 4 Stationary shock problem. In this Riemann problem the initial data are chosen in order to yield a single stationary shock, [9]. The left and right data are respectively $(\rho_L, u_L, T_L) = (1, 1.2, 0.1)$ and $(\rho_R, u_R, T_R) = (1.655, 0.725, 0.405)$.

Test 5 Space homogeneous problem. This test problem is designed to estimate the duration of the initial layer. The initial data are a space homogeneous distribution $f(x, v, t = 0) = M_1(v) + M_2(v) + M_3(v)$, where the functions M_i are Maxwellians defined through the following macroscopic

	Kn $= 10^{-1}$		
N_{v}	ρ	u	T
21	0.5798631023e-05	0.5224619275e-05	0.9207048671e-05
26	0.5783314271e-05	0.5218811861e-05	0.9203535516e-05
31	0.5795008211e-05	0.5222206621e-05	0.9206687934e-05
	Kn $= 10^{-2}$		
N_{v}	ρ	u	T
21	0.1671999661e-04	0.2671395061e-04	0.4019432389e-04
26	0.1671992934e-04	0.2671382107e-04	0.4019444948e-04
31	0.1671996246e-04	0.2671388763e-04	0.4019438255e-04
	Kn $= 10^{-5}$		
N_{v}	ρ	u	T
21	0.1702841179e-04	0.5684926667e-04	0.3485306677e-04
26	0.1702841172e-04	0.5684926655e-04	0.3485306678e-04
31	0.1702841175e-04	0.5684926661e-04	0.3485306678e-04

Table 4: Test 1, absolute errors under velocity grid refinement, MiMe2, $N_{\mathrm{x}} = 320$

variables:

$$(\rho_1, u_1, T_1) = (2, -3, 0.9) \qquad (\rho_2, u_2, T_2) = (3, 0.1, 0.3) \qquad (\rho_3, u_3, T_3) = (7, 4, 0.24).$$

The final distribution is the Maxwellian corresponding to the triplet $(\rho_\infty, u_\infty, T_\infty) = (12, 1.8583, 7.7476)$. All computations performed here with MiMe schemes, have a time step given by

$$\Delta t = 0.9 \frac{h}{\alpha}$$

where $\alpha(t) = \max_x(|u| + C)$. We recall that IMEX schemes of [42] are affected by a more severe CFL restriction, as there the time step is given by

$$\Delta t = 0.9 \frac{h}{v_M}$$

v_M being the largest microscopic velocity used in the computations. Finally, the CNS solver uses a time step given by

$$\Delta t = 0.9 \min\left(\frac{h}{\alpha}, \frac{h^2}{3\mathrm{Kn} T_M \rho_M}\right),$$

since, for Kn not too small the CNS solver becomes unstable unless the more restrictive parabolic CFL is used. Here T_M and ρ_M are the maximum temperature and density at a given time.

The α values and the largest microscopic velocities for the tests considered here are summarized in the following table:

Test ♯	α	v_M	$r = v_M/\alpha$
1	1.9330	7.8494	4.0607
2	2.8371	6.0801	2.1431
3	9.1485	33.3021	3.6402
4	2.4247	4.1535	1.7130
5	6.6788	7.4466	1.1150

	Kn = 10^{-1}		
N_v	ρ	u	T
21	1.7373903651e-06	1.3113135547e-06	1.8843548732e-06
26	1.7361755930e-06	1.3105948862e-06	1.8841892660e-06
31	1.7371437792e-06	1.3110141697e-06	1.8843907424e-06
	Kn = 10^{-2}		
N_v	ρ	u	T
21	4.6295513156e-06	5.7279642337e-06	1.1310876938e-05
26	4.6295460494e-06	5.7279480114e-06	1.1310891562e-05
31	4.6295486217e-06	5.7279564543e-06	1.1310883646e-05
	Kn = 10^{-5}		
N_v	ρ	u	T
21	4.1261908489e-06	1.4276614164e-05	8.4119019834e-06
26	4.1261908401e-06	1.4276614148e-05	8.4119019814e-06
31	4.1261908451e-06	1.4276614157e-05	8.4119019820e-06

Table 5: Test 1, absolute errors under velocity grid refinement, MiMe2, $N_\mathrm{x} = 640$

Therefore r measures the advantage in terms of number of time steps when MiMe scheme is used instead of a scheme such as BGK-IMEX which is explicit in the convective step. This gain is even more noticeable if one used a trapezoidal rule for quadrature in velocity space, since then the values of v_M would be much larger. In fact, it is worth recalling that the use of a trapezoidal rule for computing integrals over $\mathbb{R}$, requires a preliminar approximation of $\mathbb{R}$ with a finite interval, sufficiently large to disregard the tails of the distribution falling outside this computational domain. On the contrary, Gauss Hermite quadrature is already built for computing integrals over such an infinite domain, and this cut-off is not required.

Regarding the parabolic CFL restriction for the CNS solver, we remark that it becomes more and more restrictive as h decreases and/or Kn increases. For example, for the stationary shock (test 4): here, on a space grid with $N_\mathrm{x} = 800$, the time step for MiMe schemes is $\Delta t = 0.0070$ independently of the Knudsen number, whereas for the CNS solver it is $\Delta t = 0.0070$ for Kn $= 0.01$ and $\Delta t = 0.0012$ for Kn $= 0.1$.

Test 1 permits to assess the convergence rate of MiMe schemes. As reference solution, we use the third order BGK3 scheme of [42] with 1280 intervals, and 21 nodes for the Hermite quadrature in velocity space. The results appear in Table 1 for the first order scheme, and Table 2 for the second order scheme. For a comparison, the tables contain also the corresponding errors obtained with the implicit-explicit (IMEX) first and second order BGK1 and BGK2 schemes respectively, from [42]. In the tables, the errors are measured with the L^1 norm; we find similar results with the L^∞ norm, see also Figure 1. The IMEX schemes use the microscopic CFL, which is given by the fastest microscopic velocity in the Hermite grid, see the table above. The completely implicit MiMe schemes use the macroscopic CFL, which, for this test problem, allows to use time steps approximately 4 times larger. Even though the time step is considerably larger, the errors of MiMe schemes are definitely smaller than for the IMEX case in Table 1. For the second order scheme, we use the adaptive strategy for moments realignment, which acts on the finest grids, only in the last time steps, when the density profiles become sharper. Also in this case the errors obtained with the second order MiMe scheme are considerably smaller than in the IMEX case. In Table 3 we report the corresponding CPU times. It is clear that MiMe schemes provide smaller CPU times than the IMEX BGK schemes, using the same space and velocity grid, thanks to the fact that a larger time step can be chosen.

N_x	Mass	Momentum	Energy
	$\mathrm{Kn} = 10^{-1}$		
40	1.11e-17	2.33e-19	3.78e-07
80	4.18e-11	1.48e-09	2.25e-08
160	4.10e-12	5.78e-11	6.05e-10
320	5.87e-14	5.18e-13	4.04e-12
640	7.06e-16	4.07e-15	2.40e-14
	$\mathrm{Kn} = 10^{-5}$		
40	1.11e-17	2.33e-19	5.55e-18
80	2.77e-17	2.42e-19	1.11e-17
160	1.11e-17	3.43e-19	9.02e-18
320	9.02e-18	2.08e-19	0.00e-00
640	3.46e-18	3.08e-19	1.11e-17

Table 6: Test 1, errors in conservation, MiMe1

N_x	Mass	Momentum	Energy
	$\mathrm{Kn} = 10^{-1}$		
40	2.91e-11	9.51e-10	3.34e-09
80	3.28e-12	1.24e-11	6.99e-11
160	2.10e-15	1.24e-14	2.67e-14
320	1.53e-15	3.35e-18	9.74e-16
640	3.26e-15	1.30e-15	1.86e-15
	$\mathrm{Kn} = 10^{-5}$		
40	2.01e-11	3.50e-11	3.05e-11
80	2.10e-16	3.23e-16	2.92e-16
160	5.55e-18	4.61e-17	6.93e-19
320	4.99e-17	2.88e-17	4.16e-18
640	1.52e-17	3.88e-17	1.17e-17

Table 7: Test 1, errors in conservation, MiMe2

In these tables the error due to quadrature in velocity is much below the error due to the space and time discretization, even though the velocity nodes are relatively few. This is due to the high convergence rate of Gauss-Hermite quadrature formulas. To illustrate this fact, we include two tables reporting the behavior of the error on the finest grids in space and time, under velocity grid refinement. Tables 4 and 5 are computed for $N_\mathrm{x} = 320$ and $N_\mathrm{x} = 640$ respectively, refining only the grid in velocity space, i.e. increasing both the degree of the Gauss Hermite polynomials and the number of grid nodes on which the quadrature is based. They show that the refinement in velocity space acts only on the third digit of the error for $\mathrm{Kn} = 10^{-1}$, and its impact is even lower on smaller Knudsen numbers. The same behavior occurs for both values of N_x shown. Thus, even on the finest space grids we are considering, the error due to space and time truncation is much larger than the error due to quadrature in velocity. For this reason, in all the following tests we will use a Gauss-Hermite formula with 21 nodes. We will further explore the behavior of the error under velocity grid refinement in the space homogeneous case in Fig. 5.1.

Tables 6 and 7 contain the errors in conservation for the first and the second order schemes respectively, for $\mathrm{Kn} = 10^{-1}$ and $\mathrm{Kn} = 10^{-5}$. Results for $\mathrm{Kn} = 10^{-2}$ are similar. The errors in conservation are

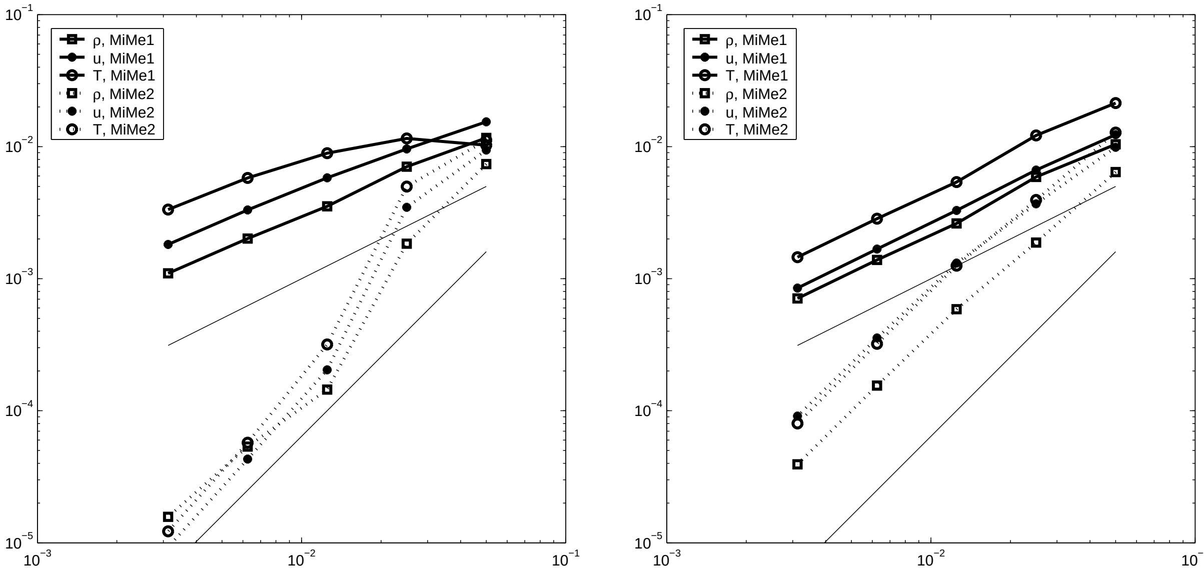

Figure 1: Test 1, errors on the macroscopic quantitites as a function of h, L^∞ norm (left: $\mathrm{Kn} = 10^{-1}$, right: $\mathrm{Kn} = 10^{-5}$), MiMe1 and MiMe2. The thin lines represent the reference slopes for first and second order convergence.

computed evaluating the difference between total mass, momentum and energy at the initial and final times. Note that in all cases the errors in conservation are by far below the truncation errors of the scheme, and very close to machine precision. Thus, even though we are not using the exact discrete Maxwellian of [34], we do not need a large number of velocity nodes to ensure conservation. This is again a consequence of the high accuracy of the Gaussian-Hermite quadrature used here, see also [1], and of the discretization of the macroscopic equations with conservative numerical fluxes.

Figure 1 shows the convergence history in the L^∞ norm on Test 1, under grid refinement in space and time, with $N_v = 21$ nodes in velocity space. It is clear that both schemes have the expected order as the grid is refined, even though the accuracy of the quadrature formula in velocity space is fixed. Again, we note that, with these parameters, the error due to velocity quadrature is lower than the error in space and time.

Figure 2 illustrates the influence of moments realignment. We plot for both the first and the second order schemes the temperature profiles for Test 2 for a large Knudsen number, $\mathrm{Kn} = 10^{-1}$. For the first order scheme moments realignment enhances convergence and reduces artificial diffusion (see top of Figure 2). For the second order scheme, the lack of moments realignment results in spurious oscillations on finer grids where gradients are sharper and therefore rarefaction effects are stronger. For smaller Knudsen numbers the influence of moments realignment is less evident and therefore is not plotted. From now on, we consider only moments realignment with $TOL = 0.01$.

Figure 3 shows the temperature profiles on Test 2 for the first and second order schemes. The enhancement of the solution obtained with the second order scheme is evident for all grids. Also note the sharpness of the shock profiles in the hydrodynamic limit for the second order scheme.

We have observed that the distribution function f remains positive for both MiMe1 and MiMe2 on the smooth test. In tests involving Riemann problems, the second order scheme MiMe2 may exhibit small undershoots in f in the first time steps, when the discontinuities in the initial data are still strong. Figure 4 exibits the evolution of the negative minima of f with time for the second order scheme, and for relatively high Knudsen numbers. The spurious minima have maximum amplitude of order 10^{-6} and

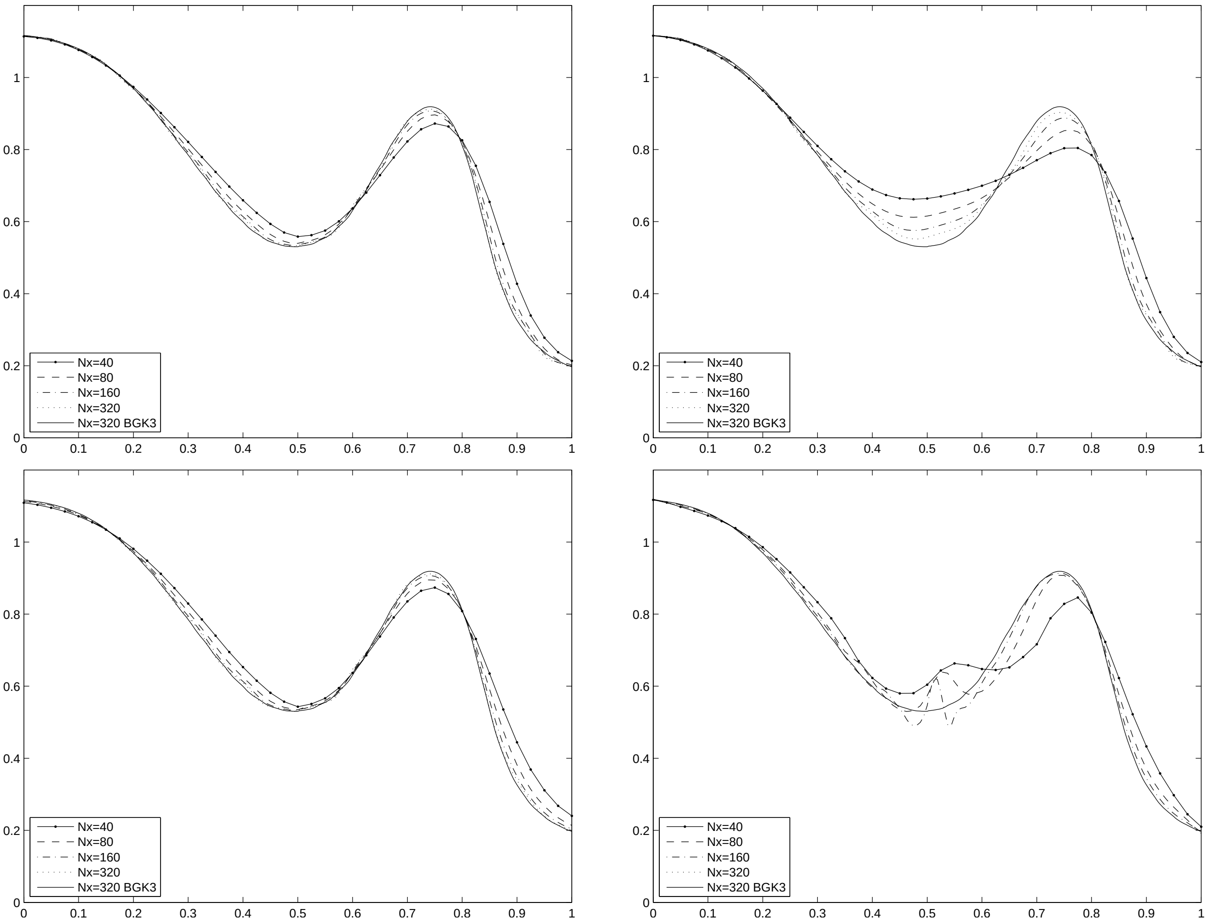

Figure 2: Test 2, temperature profiles, Kn $= 10^{-1}$. Top: MiMe1, bottom: MiMe2. Left: with moments realignment, right: without moments realignment.

it is clear that they are absorbed by the flow quite fast, and do not seem to depend strongly on the grid spacing. For smaller Knudsen numbers the decay of the spurious minima to zero may be slower, but on the other hand, the macroscopic behavior at this stage is mainly dictated by the local Maxwellian. The solution f obtained with MiMe1 instead has never exhibited spurious negative minima in the tests we tried, and in fact it is easy to prove from (16) that f^{n+1} remains positive, if f^n is positive.

An interesting quantity to monitor is the entropy, which gives indications on the dissipative properties of the schemes. Since the definition of the entropy requires, of course, a non-negative f, we must clip the spurious negative undershoots of f. Thus the entropy will be defined with the following relations:

$$\text{Let: } \widetilde{f} = \max(f, 0) \quad \Rightarrow H(f) = \left\langle \widetilde{f} \ln \widetilde{f} \right\rangle,$$

so that $\widetilde{f} \ln \widetilde{f}$ is set to zero where f is negative.

Figures 5 and 6 show the entropy decay in time for the first and the second order schemes in a smooth test (Test 1) and on a Riemann problem (Test 2).

In the smooth case (Figure 5) the entropy decay is purely numerical in the hydrodynamic limit (see right of Figure 5). The decay is approximately linear in h for the first order scheme and clearly converges

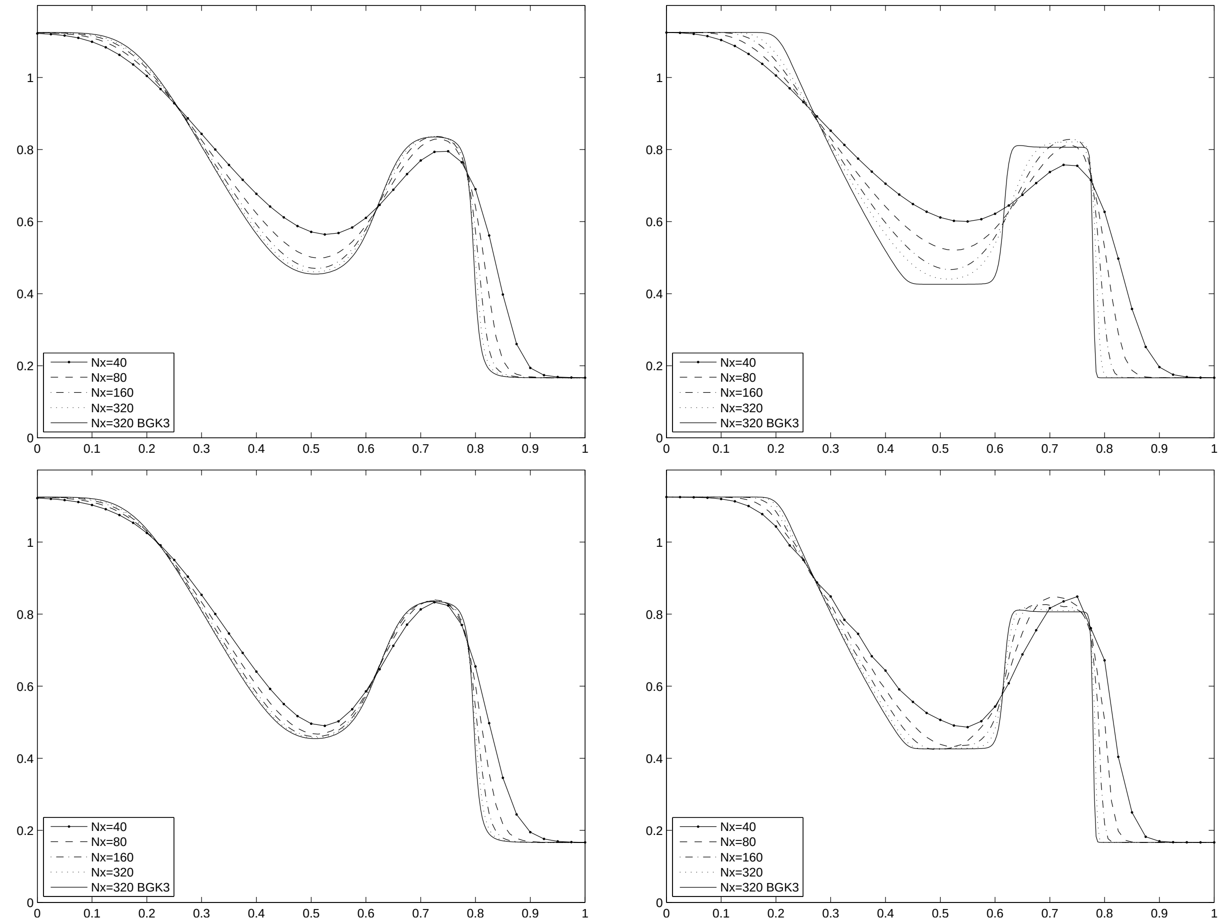

Figure 3: Test 2, temperature profiles. Top: MiMe1, bottom: MiMe2. Left: $\mathrm{Kn} = 10^{-2}$, right: $\mathrm{Kn} = 10^{-5}$.

to zero faster for the second order scheme. In the kinetic regime the entropy dissipation converges from below to its asymptotic limit, again with a faster convergence in the second order case. The extra entropy dissipation with respect to the asymptotic solutions is due to the numerical dissipation of the scheme.

For the Riemann problem entropy dissipation is nonzero even in the hydrodynamic regime due to entropy production across shocks. This appears clearly in Figure 6 in which the scale on the y axis has a wider range than in the smooth case. Still convergence occurs from below indicating that the schemes are entropy stable.

Figure 7 contains the density profiles for the Lax shock tube problem in the hydrodynamic regime. This test is a classic benchmark for computational gasdynamic and it is known to be quite a hard problem. Both the first and the second order schemes reproduce the solution remarkably well even on the extremely coarse $N_{\mathrm{x}} = 40$ grid. The presence of small oscillations whose amplitude decreases under grid refinement is well known also for high order Euler solvers.

Figures 8 and 9 show the density, macroscopic velocity, temperature and entropy decay for $\mathrm{Kn} = 10^{-1}$ and $\mathrm{Kn} = 10^{-2}$, respectively, for the second order scheme on Test 3. The coarse grid clearly gives very inaccurate results, which however improve if moments realignment is applied with a stricter tolerance. The bad behavior of the coarse grid is not surprising: a typical number of grid points for gas dynamics

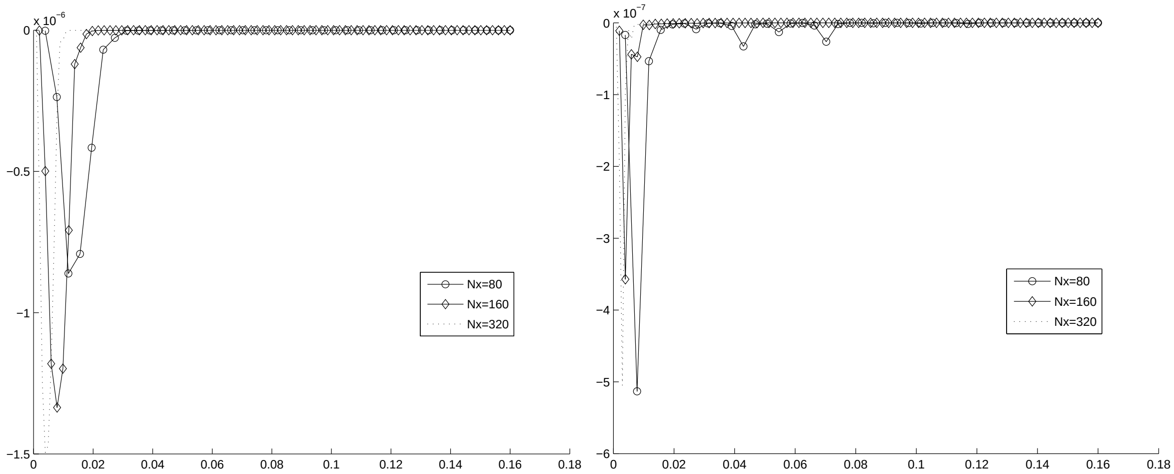

Figure 4: Test 2, minima of f over x and v as a function of time, MiMe2, $\mathrm{Kn} = 10^{-1}$ (left) and $\mathrm{Kn} = 10^{-2}$ (right)

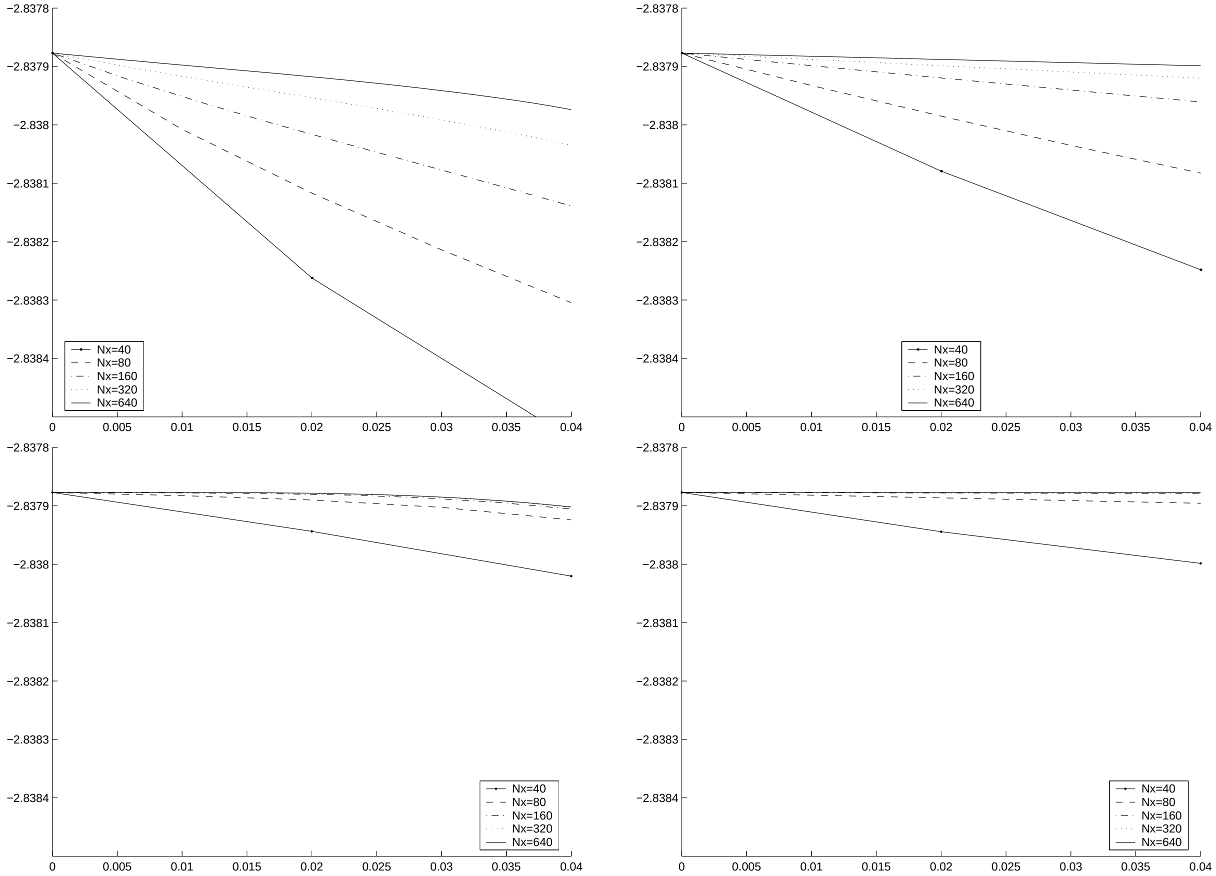

Figure 5: Test 1 (smooth case), entropy decay as a function of time for several grids. Top: MiMe1, bottom: MiMe2. Left: $\mathrm{Kn} = 10^{-1}$, right: $\mathrm{Kn} = 10^{-5}$.

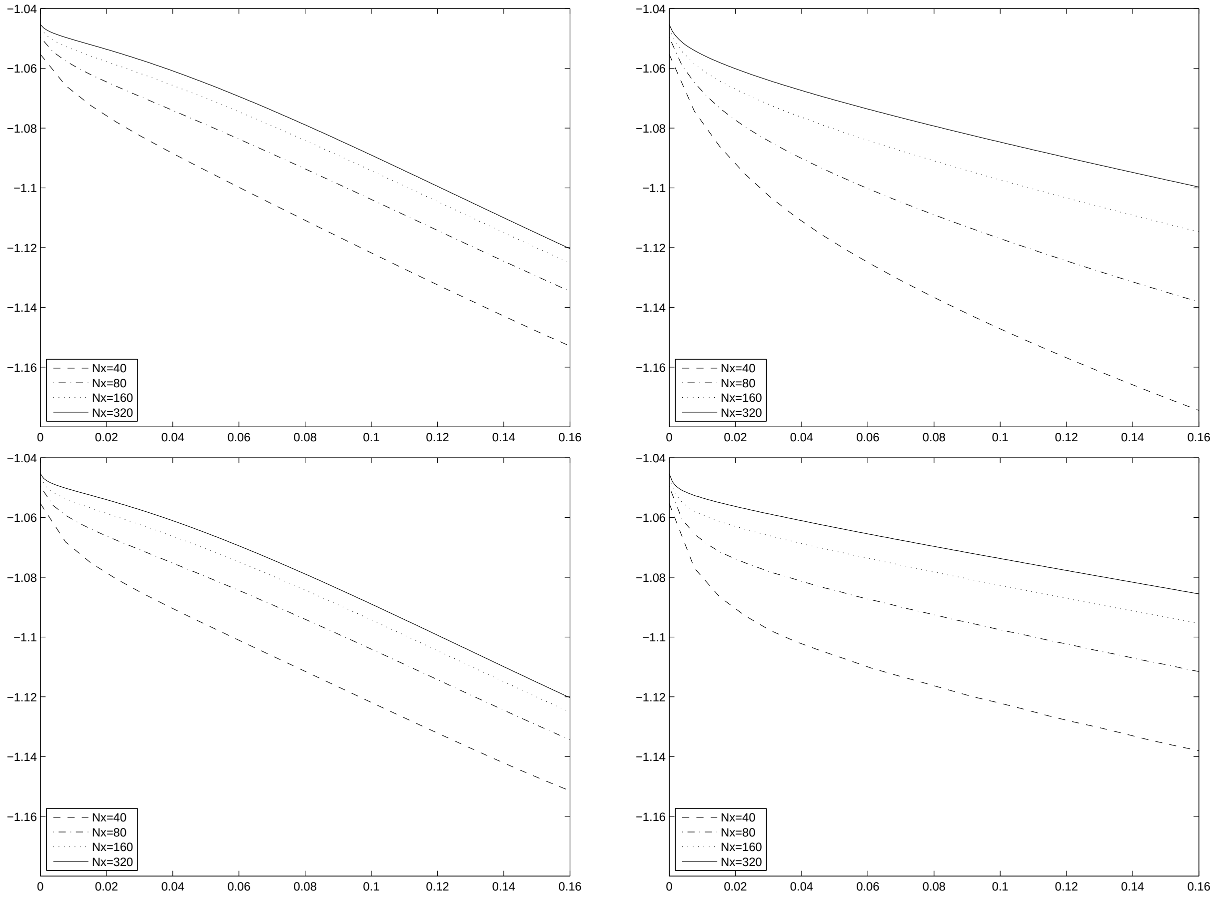

Figure 6: Test 2 (Riemann problem), entropy decay as a function of time for several grids. Top: MiMe1, bottom: MiMe2. Left: $\mathrm{Kn} = 10^{-1}$, right: $\mathrm{Kn} = 10^{-5}$.

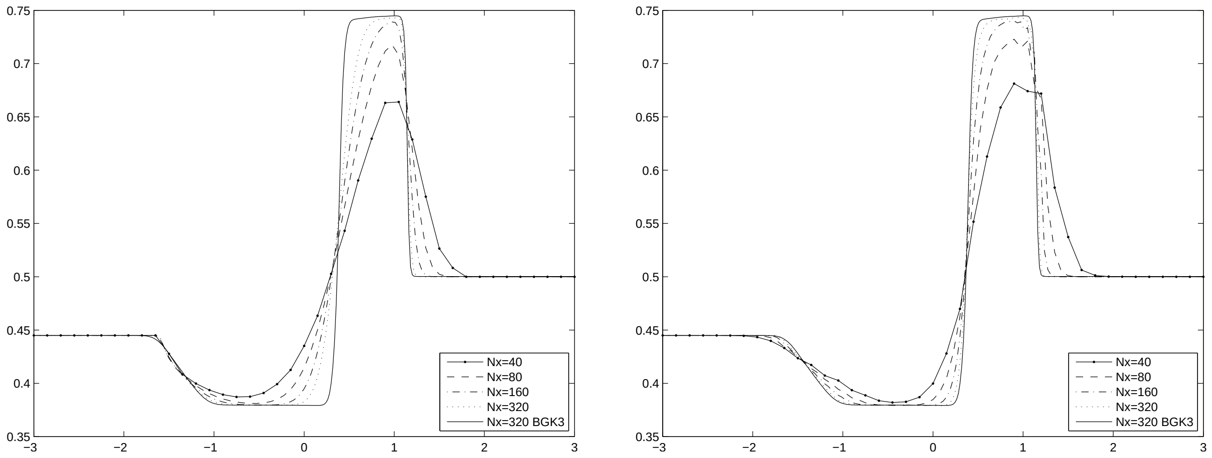

Figure 7: Test 3, density profiles, $\mathrm{Kn} = 10^{-5}$. Left: MiMe1, right: MiMe2.

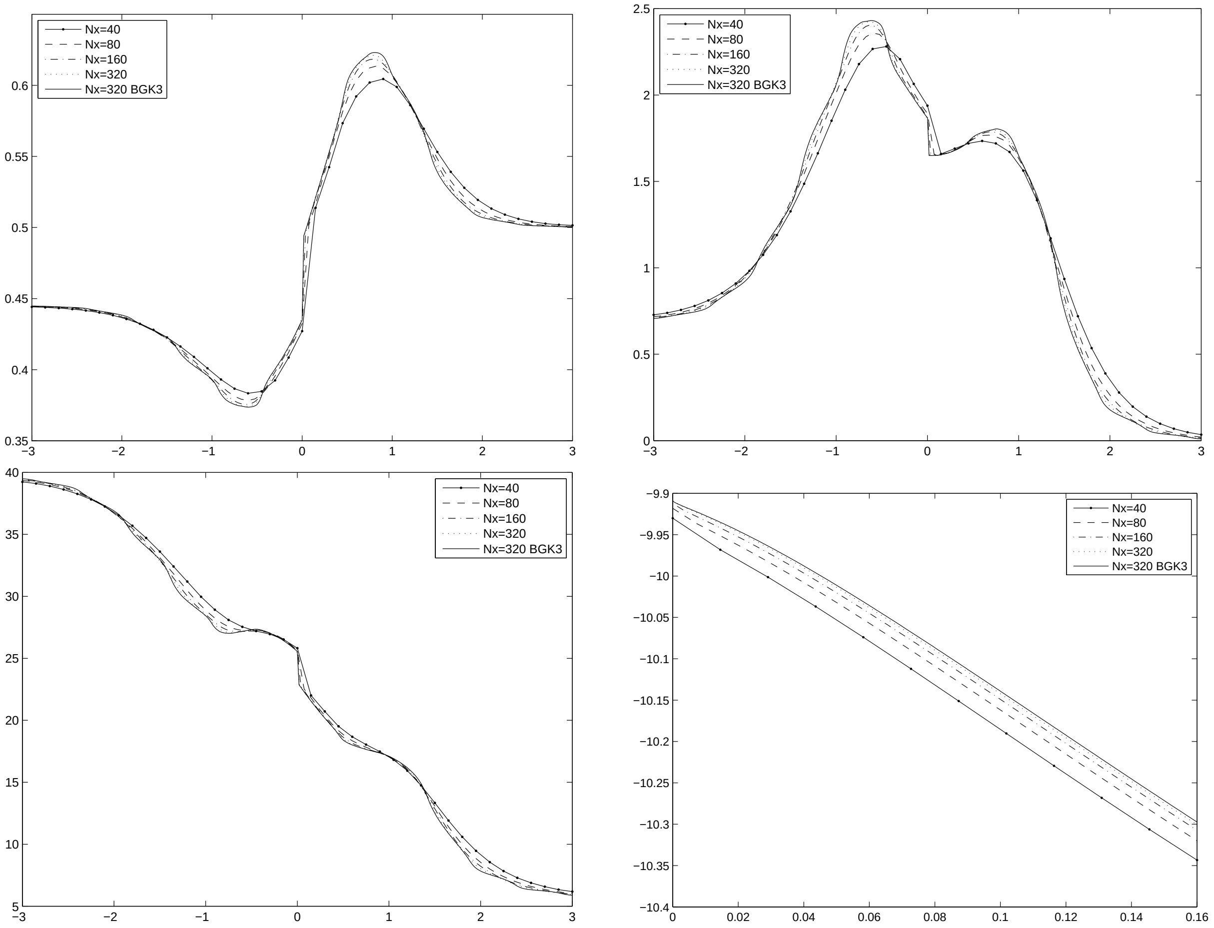

Figure 8: Test 3, $\mathrm{Kn} = 10^{-1}$, MiMe2. Left to right and top to bottom: ρ, u, T, and entropy decay for several grids.

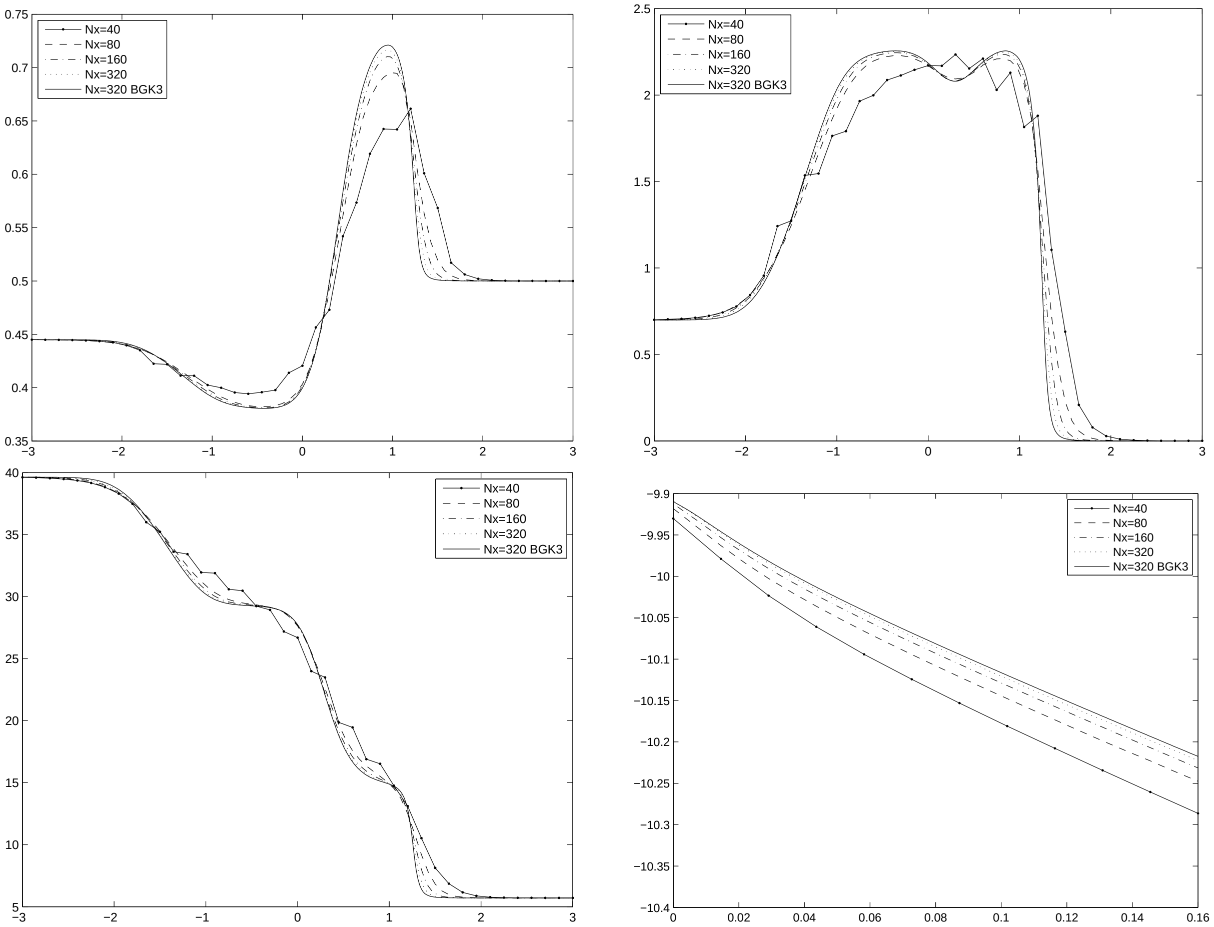

Figure 9: Test 3, Kn $= 10^{-2}$, MiMe2. Left to right and top to bottom: ρ, u, T, and entropy decay for several grids.

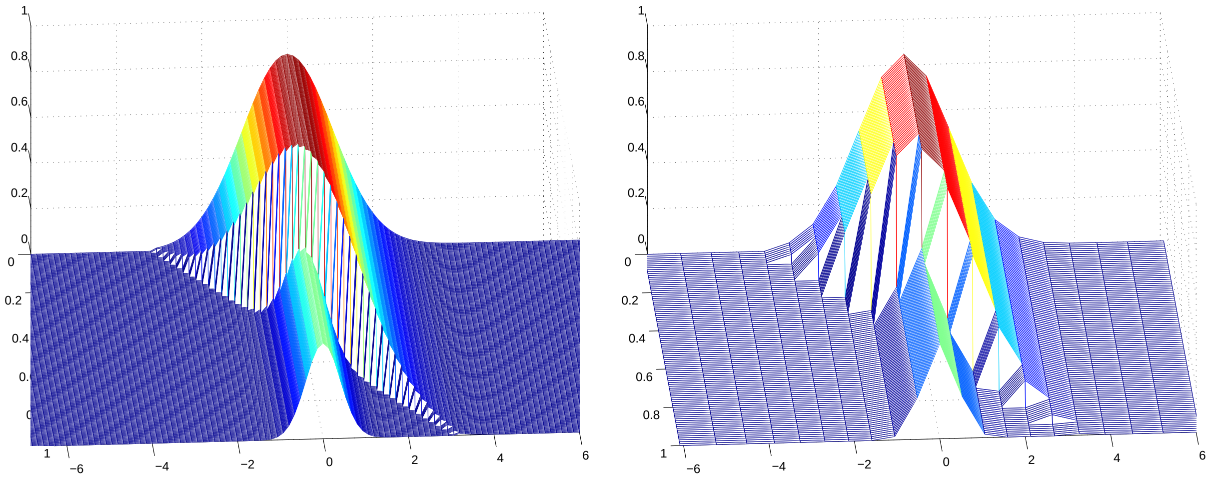

Figure 10: Free advection of the Riemann problem of Test 2. Solution on a fine grid (left) and projection on the coarse velocity grid used by MiMe schemes (right).

computations of this test is above 100 nodes. The plots give indications on the evolution of Lax initial data for a rarefied gas. It is interesting to see that the solution exhibits a rich structure which shows the need of limiters even in the rarefied regimes, and in fact the solution becomes unstable if the limiters are turned off.

We also explore the high Knudsen behavior of MiMe schemes. Fig. 10 shows the collisionless solution of the Riemann problem of Test 2, in the limit of $\mathrm{Kn} \to \infty$. Note the presence of discontinuities in f which is particularly apparent on a fine velocity grid. The left panel of Fig. 11 shows the collisionless solution computed with a second order upwind flux which is clearly the solution that MiMe schemes will converge to for high Kn. On the right, we plot the solution computed by MiMe2 for $\mathrm{Kn} = 1$. Since the computational domain is $L = 1$, this value of the Knudsen number corresponds roughly to one collision per unit time, and thus relaxation effects are negligible. It is apparent that MiMe2 is able to capture the correct free flow limit without oscillations. We think that the schemes easily capture the correct limit, because the whole distribution function is evolved with time, rather than only the kinetic projection, as occurs for instance in [9].

In all the tests shown above, the numerical flux was the Lax Friedrichs numerical flux, given by (12). This numerical flux is known to be robust, but highly diffusive. In Figure 12 we compare the solutions obtained with the Lax Friedrichs numerical flux in the macroscopic equations, with the solution obtained using the HLL flux (13), which is less diffusive, for several Knudsen numbers and two values of N_{x}. The figure shows that the profiles almost coincide in kinetic regimes, while the HLL flux gives distinctively less diffusive profiles for smaller Knudsen numbers. We will use the HLL flux for studying the approximation of the Navier Stokes regime, where a good resolution is a key aspect. However note that even the Lax Friedrichs flux gives good results.

5.1 Shock structure, CNS asymptotics and initial layer

In this section we study the behavior of MiMe kinetic schemes in the asymptotic regime of small, but not vanishing, Knudsen numbers. Figure 13 shows the shock thickness of the shock wave contained in the numerical solution of Test 2. To evaluate the shock thickness, we measure the length of the interval along which the central 80% of the jump in the shock is spread. On the left of Figure 13, we plot the shock thickness as a function of the Knudsen number for several grid values. The vertical lines correspond

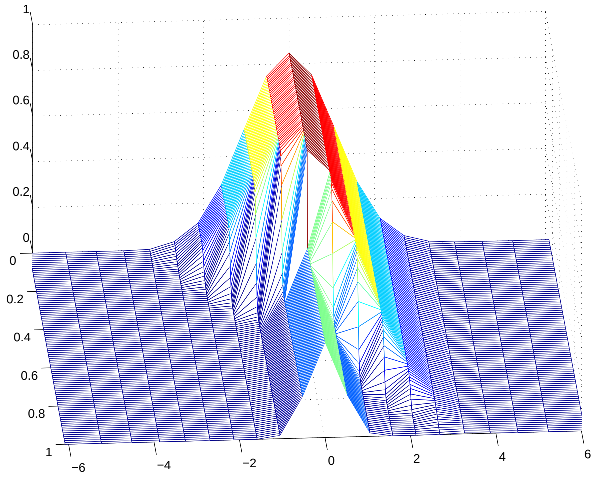

Figure 11: Free flow solution for Test 2 computed with a second order upwind flux (left). Corresponding computed f for $\mathrm{Kn} = 1$ with MiMe2 (right).

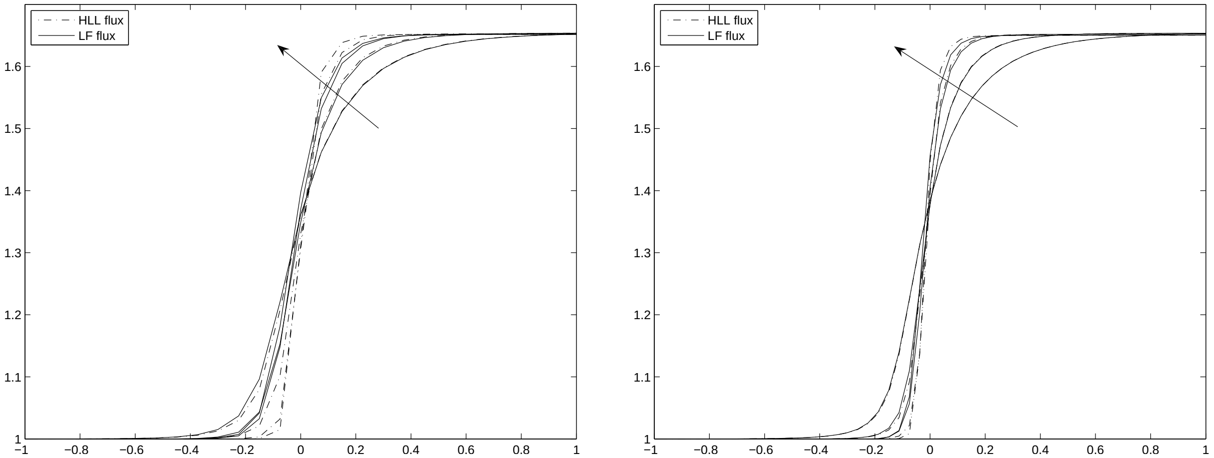

Figure 12: Test 4, comparison of Lax-Friedrichs (solid lines) and HLL (dashed line) numerical fluxes on the density profiles, MiMe2, for $\mathrm{Kn} = 0.1, 0.05, 0.02, 0.01$ and $N_{\mathrm{x}} = 200$ (left) and $N_{\mathrm{x}} = 400$ (right). The direction of the arrows indicates values of Kn decreasing.

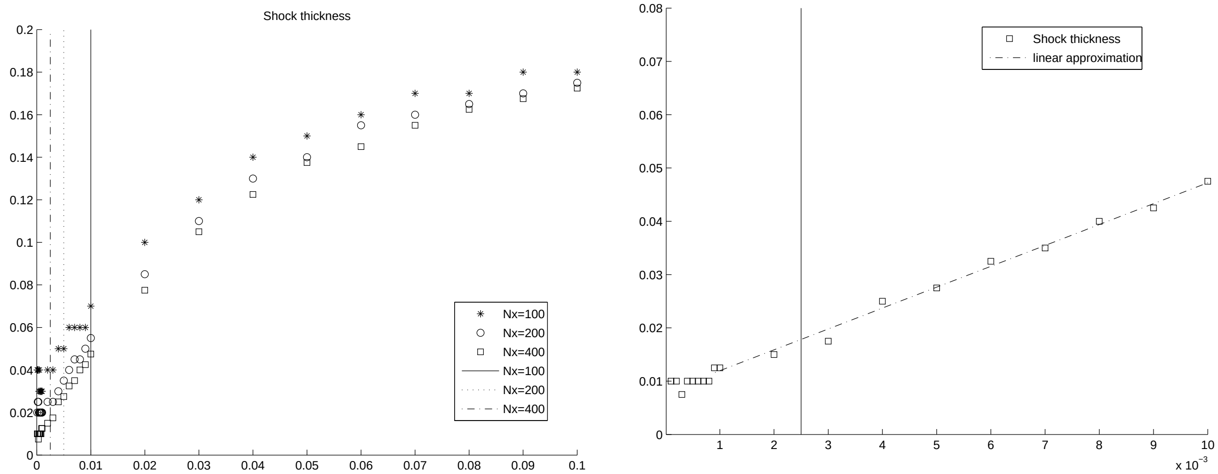

Figure 13: Test 2, shock thickness as a function of Kn for several values of N_{x}, MiMe2 (left). Right: zoom of the case $N_{\mathrm{x}} = 400$ with the corresponding linear regression line. The vertical lines correspond to the different values of h.

to the values of h used, and they represent the limit under which the corresponding grid is not able to resolve the shock structure. It is apparent that the shock thickness decreases approximately linearly, as Knudsen is decreased below a certain threshold. The right of Figure 13 shows the linear regression line superposed to the data given by the finest grid. The agreement is excellent, and shows that the shock thickness is indeed a linear function of the Knudsen number in this regime.

Figure 14 shows a comparison between the distribution function and the local Maxwellian, as a function of v within the three waves of the solution of the Riemann problem of Test 2. Results are obtained with MiMe2 on a space grid with $N_{\mathrm{x}} = 320$. In the most rarefied regime, top left, it is clear that the gas is still not in equilibrium in all cases. For $\mathrm{Kn} = 10^{-2}$ the gas is almost at equilibrium in the rarefaction and contact waves, but still far from equilibrium within the shock. Local equilibrium in all three waves, with these data and with the resolution power of the grid used, is achieved only for $\mathrm{Kn} = 10^{-5}$ (bottom right), when f coincides with the local Maxwellian even in the shock.

We also explore the time length of the initial layer. We consider a space homogeneous problem (Test 5), and we plot the distance of f from the final steady Maxwellian M_∞ as a function of time, namely $||f(.,.,t) - M_\infty(.,.,t)||$, for several values of the Knudsen number. The results shown in Figure 15 correspond to data obtained with MiMe1 and MiMe2 on a space time grid with $N_{\mathrm{x}} = 200$ and $\Delta t = 6.6667 \cdot 10^{-4}$, and are very similar. From each curve, it is possible to derive the corresponding half-life of the transient, which is approximately linear in the Knudsen numbers, as long as the Knudsen number is large enough to be resolved by the time step used.

In this test problem, the dependence on the velocity grid can be studied, without the influence of the space discretization error, which in our tests, is always larger. Fig 5.1 shows the convergence of the error under velocity grid refinement. As expected, the rate is exponential, as shown by the excellent fit with an exponential rate on the right of the figure.

Finally, we compare the results obtained by the kinetic scheme, with a Compressible Navier Stokes solution on a stationary shock. In Figure 17, the dashed line represents the shock solution given by the Compressible Euler equations, the solid line is the numerical solution of the CNS equations (31), obtained with an explicit discretization based on the HLL flux for the convective terms, and a centered formula for the diffusive term. The remaining curves are obtained with MiMe2, also with the HLL flux, on the BGK equations, for several grids. For $\mathrm{Kn} = 0.1$, the solution is still kinetic, and converges towards a

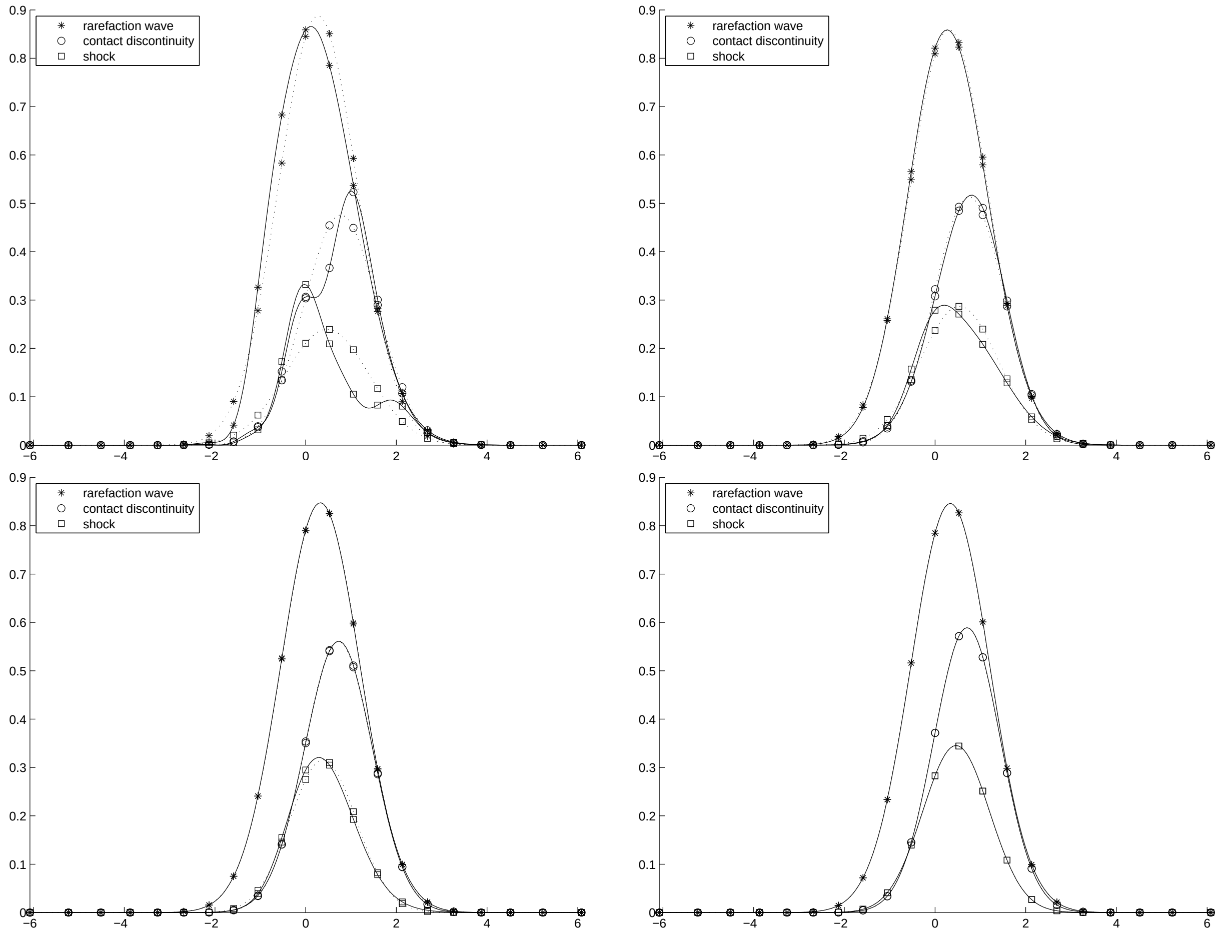

Figure 14: Test 2, distribution function f (solid line) and local Maxwellian (dotted line) versus v, MiMe2. Left to right and top to bottom: $\mathrm{Kn} = 10^{-1}$, $\mathrm{Kn} = 10^{-2}$, $\mathrm{Kn} = 10^{-3}$, $\mathrm{Kn} = 10^{-5}$

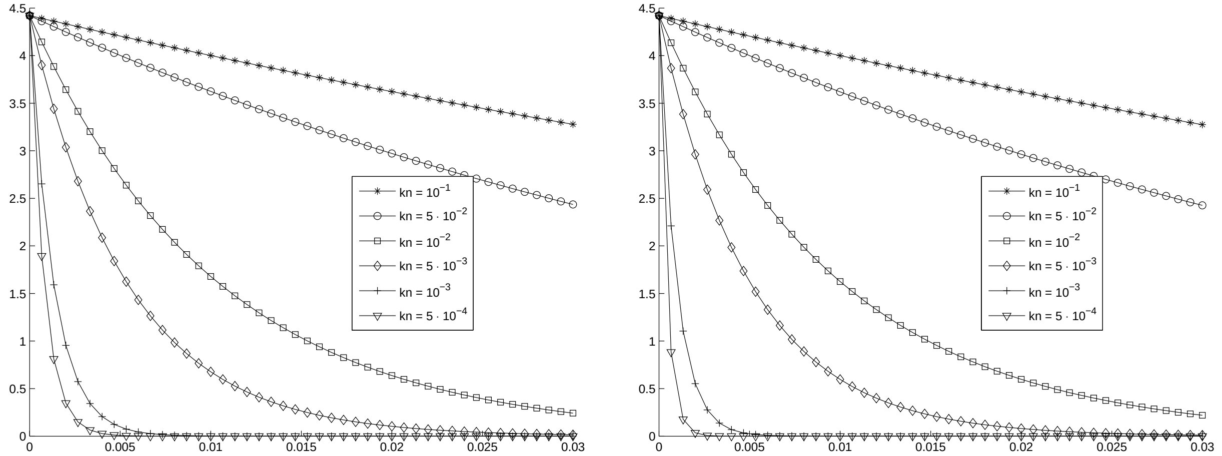

Figure 15: Test 5, relaxation to equilibrium as a function of time. Left: MiMe1; right: MiMe2

N_{v}	ρ	u	T	v_M
16	7.9415e-03	7.0111e-04	6.2624e-03	5.5478
21	2.1884e-04	1.8900e-05	2.7746e-04	6.5673
26	7.4381e-06	1.9639e-06	3.1381e-06	7.4656
31	9.2759e-09	5.5894e-08	2.7967e-07	8.2774

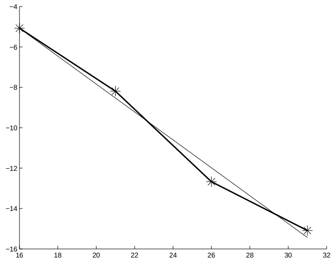

Figure 16: Space homogeneous problem (Test 5), absolute errors versus number N_v of velocity grid nodes, MiMe2. Left, actual errors and maximum grid velocity. Right, convergence speed (log scale): the continuous straight line corresponds to an exponential rate.

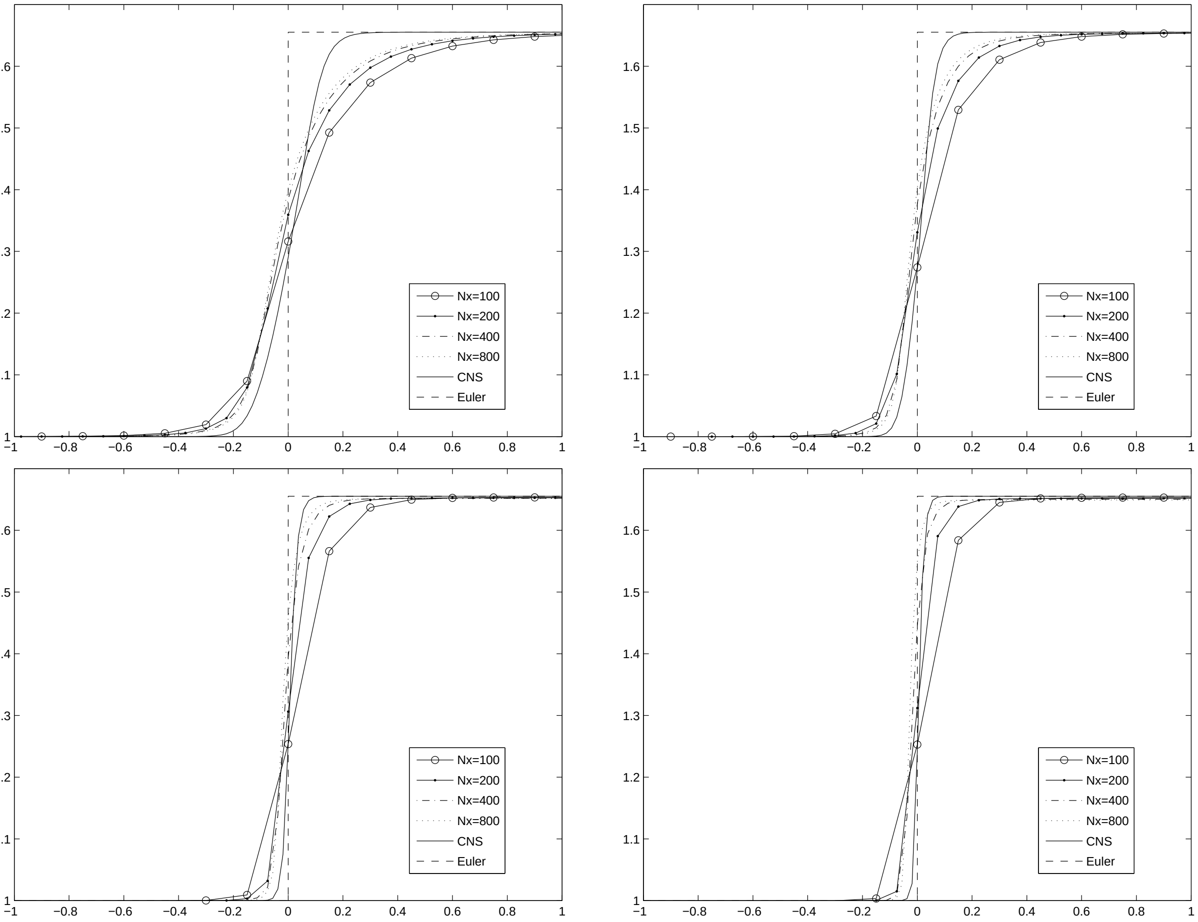

Figure 17: Test 4, convergence to Compressible Navier-Stokes, density profiles, MiMe2. Left to right, top to bottom: Kn = 0.1, Kn = 0.05, Kn = 0.02 and Kn = 0.01

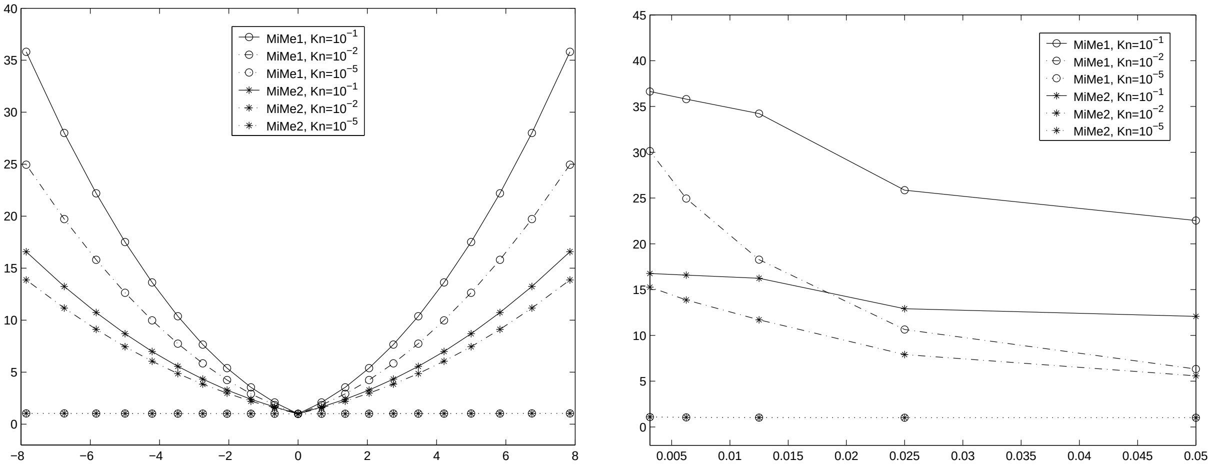

Figure 18: Condition number of the matrix defining the linear systems (16) and (23) versus v for $N_{\mathrm{x}} = 320$ (left) and versus h for $v = \max_k |v_k|$ (right)

profile which is far from both Euler and CNS solutions. Reducing Kn we clearly see that the MiMe solution approaches the CNS profile, which, in turn, is converging towards Euler solution. These profiles correspond to values of Kn which are still away from the hydrodynamic regime. It is clear that the solutions obtained with MiMe2 are closer to the Navier Stokes profile rather than to the Euler shock wave.

5.2 Condition number

Finally, Figure 18 shows the behavior of the condition number of the matrices defining the linear systems (16) and (23) as a function of microscopic velocity values for a fixed h ($N_{\mathrm{x}} = 320$, left) and as a function of h for a fixed v ($v = \max_k |v_k|$, right), for several Knudsen numbers and for both the first and the second order schemes. Here both schemes are fully implicit, with $\theta_k \equiv 1$. It is clear that, for a fixed space grid, the condition number increases as v increases, but still remaining small in all cases, and actually approaching 1 in the hydrodynamic regime. On the other hand, for a fixed value of v, the conditioning of the matrix gets worse as the grid is refined, though the increase is by far sub-linear, and again the actual values remain small. Despite these data are obtained on problems with one degree of freedom in velocity, these results can be generalized to fully 3D problems simulating a real monoatomic gas. In fact the general case contains the sum of three velocity operators which have the same structure and therefore the same eigenvalues of the 1D problem. The coefficient matrix for the fully 3D case will have a banded structure requiring the use of iterative solvers. However these results show that the resulting matrix is well-conditioned and therefore the system is easily solvable e.g. with a few GMRES iterations.

6 Conclusions and perspectives

In this work, we have presented first and second order accurate schemes to integrate the BGK kinetic model. The schemes proposed are characterized by evolving the macroscopic variables explicitly and the distribution function implicitly (MiMe schemes). With the technique proposed, the evolution of the local Maxwellian is computed explicitly, and therefore the system of equations for the implicit values of the distribution function becomes linear. Moreover, the whole construction is subject to a stability restriction linked to the macroscopic velocity and sound speed, which coincides with the classical CFL condition of Euler equations. For this reason, the schemes proposed are particularly indicated for hybrid schemes based on a domain decomposition in which the BGK model is used to solve the problem in rarefied regimes, while Navier-Stokes or Euler are used for small Knudsen numbers [19, 21, 2]: MiMe schemes allow to use the same time step in the whole computational domain, thus minimizing spurious interface effects.

Another aspect we wish to underline is the treatment of implicit limiting in the second order MiMe scheme. It is well known that second and higher order schemes must be non linear, even for the linear advection equation, to prevent the onset of spurious oscillations in the presence of discontinuities. This fact has always hindered the application of implicit time integration for conservation laws, since non linear limiting would result in a non linear system of equations, see for instance [22]. We believe that the technique adopted here, based on lower order prediction to determine non oscillatory stencils, might be of interest also to develop implicit schemes for conservation laws with stiff propagation speeds, as in low Mach number gas dynamics, see for instance [20]. A work in this direction is in preparation.

Further investigation will involve two dimensional problems and a more realistic 3D space for the microscopic velocities, taking into account the reduction of variables found in [15], and the extension of the scheme to the ES-BGK model, where the stiffness due to the relaxation term has already been addressed in [24] and [2].

References

[1] A. Alaia, S. Pieraccini, and G. Puppo, *Velocity discretization in numerical schemes for BGK equations*, in Hyperbolic Problems: Theory, Numerics, Applications, S. Benzoni-Gavage and D. Serre, eds., Springer, 2008, pp. 857–864.

[2] A. Alaia and G. Puppo, *A hybrid method for hydrodynamic-kinetic flow, part II: Coupling of hydrodynamic and kinetic models*, J. Comp. Phys., submitted.

[3] ——, *A hybrid method for hydrodynamic-kinetic flow, part I: Reduction of stochastic noise in DSMC simulations*, J. Comp. Phys., (2011).

[4] P. Andries, K. Aoki, and B. Perthame, *A consistent BGK-type model for gas mixtures*, Journal of Statistical Physics, 106 (2002), pp. 993–1018.

[5] P. Andries, J. F. Bourgat, P. Le-Tallec, and B. Perthame, *Numerical comparison between the Boltzmann and ES-BGK models for rarefied gases*, Computer and Methods in Applied Mathematics and Engineering, 31 (2002), p. 3369.

[6] P. Andries, B. Perthame, P. Le-Tallec, and J. Perlat, *The Gaussian BGK model of Boltzmann equation with small Prandtl number*, European Journal of Mechanics - B/Fluids, 19 (2000).

[7] K. Aoki, K. Kanba, and S. Takata, *Numerical analysis of a supersonic rarefied flow past a flat plate*, Physics of Fluids, 9 (1997), pp. 1144–1161.

[8] K. Aoki, Y. Sone, and T. Yamada, *Numerical analysis of gas flows condensing on its plane condensed phase on the basis of kinetic theory*, Physics of Fluids A, 2 (1990), pp. 1867–1878.

[9] M. Bennoune, M. Lemou, and L. Mieussens, *Uniformly stable numerical schemes for the Boltzmann equation preserving the compressible Navier-Stokes asymptotics*, J. Comput. Phys., 227 (2008), pp. 3781–3803.

[10] P. L. Bhatnagar, E. P. Gross, and M. Krook, *A model for collision processes in gases. Small amplitude processes in charged and neutral one-component systems*, Physical Reviews, 94 (1954), pp. 511–525.

[11] G. A. Bird, *Molecular Gas Dynamics and the Direct Simulation of Gas Flows*, Oxford University Press, 1994.

[12] G. L. Caraffini, M. Groppi, and G. Spiga, *On BGK approximation for reactive and nonreactive flows*, Transport Theory Statist. Phys., 36 (2007), pp. 475–494.

[13] C. Cercignani, *Rarefied Gas Dynamics, from Basic Concepts to Actual Calculations*, Cambridge University Press, Cambridge, 2000.

[14] C. Cercignani, R. Illner, and M. Pulvirenti, *The mathematical theory of dilute gases*, vol. 106 of Applied Mathematical Sciences, Springer-Verlag, 1994.

[15] C. K. Chu, *Kinetic-theoretic description of the formation of a shock wave*, Physics of Fluids, 4 (1965), pp. 12–22.

[16] F. Coron and B. Perthame, *Numerical passage from kinetic to fluid equations*, SIAM J. Numer. Anal., 28 (1991), pp. 26–42.

[17] N. Crouseilles, P. Degond, and M. Lemou, *A hybrid kinetic/fluid model for solving the gas dynamics Boltzmann-BGK equation*, Journal of Computational Physics, 199 (2004), pp. 776–808.

[18] P. Degond, G. Dimarco, and L. Pareschi, *The moment guided Monte Carlo method*, International Journal for Numerical Methods in Fluids, (2010).

[19] P. Degond, S. Jin, and L. Mieussens, *A smooth transition model between kinetic and hydrodynamic equations*, Journal of Computational Physics, 209 (2005), pp. 665–694.

[20] P. Degond and M. Tang, *All speed scheme for the low Mach number limit of the Isentropic Euler equation*, Communications in Computational Physics, 10 (2011), pp. 1–31.

[21] G. Dimarco and L. Pareschi, *Hybrid multiscale methods II. kinetic equations*, SIAM Multiscale Modeling and Simulation, 6 (2007), pp. 1169–1197.

[22] K. Duraisamy and J. D. Baeder, *Implicit scheme for hyperbolic conservation laws using nonoscillatory reconstruction in space and time*, SIAM J. Sci. Comput., 29 (2007), pp. 2607–2620.

[23] F. Filbet and S. Jin, *A class of asymptotic-preserving schemes for kinetic equations and related problems with stiff sources*, J. Comput. Phys., 229 (2010), pp. 7625–7648.

[24] ——, *An asymptotic preserving scheme for the ES-BGK model of the Boltzmann equation*, J. Sci. Comput., 46 (2011), pp. 204–224.

[25] A. Frezzotti, *A numerical investigation of the steady evaporation of a polyatomic gas*, European Journal of Mechanics, B/Fluids, 26 (2007), pp. 93–104.

[26] S. Gottlieb, C.-W. Shu, and E. Tadmor, *Strong stability-preserving high-order time discretization methods*, SIAM Rev., 43 (2001), pp. 89–112.

[27] Z. Guo, T. S. Zhao, and Y. Shi, *Simple kinetic model for fluid flows in the nanometer scale*, Physical Review E, 71 (2005), pp. 035301–1, 035301–4.

[28] L. H. Holway, *Kinetic Theory of Shock Structure using an Ellipsoidal Distribution Function*, Academic Press, 1966, pp. 193–215.

[29] S. Jin, *Efficient asymptotic-preserving (AP) schemes for some multiscale kinetic equations*, SIAM J. Sci. Comp., 21 (1999), pp. 441–454.

[30] G. Karniadakis, A. Beskok, and N. Aluru, *Microflows and nanoflows : fundamentals and simulation*, Springer, New York, 2005.

[31] C. A. Kennedy and M. H. Carpenter, *Additive Runge-Kutta schemes for convection-diffusion-reaction equations*, Applied Numerical Mathematics, 44 (2003), pp. 139–181.

[32] M. Lemou and L. Mieussens, *A new asymptotic preserving scheme based on micro-macro formulation for linear kinetic equations in the diffusion limit*, SIAM Journal on Scientific Computing, 31 (2008), pp. 334–368.

[33] R. J. LeVeque, *Numerical methods for conservation laws*, Lectures in Mathematics ETH Zürich, Birkhäuser Verlag, Basel, second ed., 1992.

[34] L. Mieussens, *Discrete velocity model and implicit scheme for the BGK equation of rarefied gas dynamics*, Mathematical Models and Methods in Applied Sciences, 10 (2000), pp. 1121–1149.

[35] ——, *Schemes for Boltzmann-BGK equation in plane and axisymmetric geometries*, Journal of Computational Physics, 162 (2000), pp. 429–466.

[36] R. Monaco, M. Pandolfi Bianchi, and A. J. Soares, *BGK-type models in strong reaction and kinetic chemical equilibrium regimes*, J. Phys. A: Math. Gen., 38 (2005), pp. 10413–10431.

[37] H. Neunzert and J. Struckmeier, *Particle methods for the Boltzmann equation*, Acta Numerica, (1995), pp. 417–457.

[38] L. Pareschi and G. Russo, *Numerical solution of the Boltzmann equation I: Spectrally accurate approximation of the collision operator*, SIAM J. Numerical Analysis, 37 (2000), pp. 1217–1245.

[39] ——, *An introduction to Monte Carlo methods for the Boltzmann equation*, in ESAIM: Proceedings, vol. 10, 2001, pp. 35–75.

[40] ——, *An introduction to the numerical analysis of the Boltzmann equation*, Riv. Mat. Univ. Parma, 4** (2005), pp. 145–250.

[41] B. Perthame, *Global existence to the BGK model of Boltzmann equation*, Journal of Differential Equations, 82 (1989), pp. 191–205.

[42] S. Pieraccini and G. Puppo, *Implicit-Explicit schemes for BGK kinetic equations*, Journal of Scientific Computing, 32 (2007), pp. 1–28.

[43] G. Russo and F. Filbet, *Semilagrangian schemes applied to moving boundary problems for the BGK model of rarefied gas dynamics*, Kinet. Relat. Models, 2 (2009), pp. 231–250.

[44] L. Saint-Raymond, *From the BGK model to the Navier-Stokes equations*, Ann. Scient. Éc. Norm. Sup., 4^e série, t. 36 (2003), pp. 271–317.

[45] S. Succi, *The Lattice Boltzmann Equation for Fluid Dynamics and Beyond*, Oxford University Press, 2001.

[46] E. F. Toro, *Riemann solvers and numerical methods for fluid dynamics*, Springer, 2009.

[47] W. G. Vincenti and C. H. Kruger, *Introduction to physical gas dynamics*, Krieger, 1986.

[48] K. Xu, *A gas-kinetic BGK scheme for the Navier-Stokes equations and its connection with artificial dissipation and Godunov method*, Journal of Computational Physics, 171 (2001), pp. 289–335.

[49] K. Xu and J. C. Huang, *A unified Gas-Kinetic scheme for continuum and rarefied flows*, Journal of Computational Physics, 229 (2010), pp. 7747–7764.

[50] J. Y. Yang and J. C. Huang, *Rarefied flow computations using nonlinear model Boltzmann equations*, Journal of Computational Physics, 120 (1995), pp. 323–339.